Doctor of Philosophy

Synthesis, Structural Thermal Stability, and Thermoelectric Properties of Layered GaTe-based Single Crystals

The Graduate School of the University of Ulsan

Department of Physics

Thi Hoa Vu

Synthesis, Structural Thermal Stability, and Thermoelectric Properties of Layered GaTe-based Single Crystals

Supervisor: Sunglae Cho

A Dissertation
Submitted to
the Graduate School of the University of Ulsan
In partial Fulfillment of the Requirements
for the Degree of
Doctor of Philosophy
by
Thi Hoa Vu

August 2021

The Graduate School of the University of Ulsan

Department of Physics

This certifies that the dissertation/thesis
of Thi Hoa Vu is approved.

Soon Cheol Hong

Committee Chair, Prof. Soon-Cheol Hong

조성래

Committee Member, Prof. Sunglae Cho

Committee Member, Prof. Jungdae Kim

신 영 한

Committee Member, Prof. Young Han Shin

Committee Member, Prof. Su Dong Park

The Graduate School of the University of Ulsan

August 2021

Acknowledgement

This thesis has been achieved in University of Ulsan, South Korea. First, I would like to thank the staff of the Physics Department for supporting a professional and pleasant working environment for students.

Most especially, I would like to express my deep gratitude to my supervisor, Prof. Sunglae Cho, who gave me an opportunity to study and experience life in Korea. Thank you for your endless supports and fruitful advice over the past years.

I also would like to thank Dr. Van Quang Nguyen for reviewing my academic writing and for giving useful suggestions in my papers.

I am very grateful to Dr. Anh Duc Nguyen, Dr. Chinh Tam Le, Dr. Khac Top Le, and Dr. Van Tam Tran for their devoted help throughout the years. Especially, these guys also inspired me in scientific research as well as developing myself.

I sincerely thank Prof. Yong Soo Kim, Dr. Jong Ho Park, and Dr. Su Dong Park, who supported the resources for characterizing my samples.

I also want to express a great appreciation to my lab members and my friends, whom I have lived and studied together. I consider myself fortunate to undergo an unforgettable period with them.

A special obligation should be given to my parents, my younger brother, and my younger sister for their unconditional love and support. Especially, I would like to thank my deceased father. His advice is the luggage and the motivation for me to pass over the past time. Finally, I would like to thank my love for his marvelous empathy and encouragement.

Abstract

The emerging global energy crisis and climate change have intensified interest in clean and renewable energy sources, such as solar cells and thermoelectricity – one of the key ideas for addressing energy and climate challenges. Thermoelectric (TE) modules enable a direct conversion between waste thermal energy and useful electricity and vice versa. The abundant waste heat can come from various sources, *e.g.*, combustion of fossil fuels or as a by-product of chemical reactions and nuclear decay, indicating a significant role in power generation as well as energy conversion of TE materials.

In this century, layered materials have truly revolutionized TE research with outstanding properties as well. Particularly, the bonding heterogeneity between the intralayer and interlayer induces a significant anisotropy in mechanical, electrical, and thermal properties. By manipulating these anisotropic behaviors, it is easily enabling decouple and optimize the TE parameters, thereby achieving excellent performance.

Likewise, gallium telluride (GaTe) owns a monoclinic layered structure with strong covalent in-plane and weak van der Waals (vdW) out-of-plane bonding. Each single-crystalline layer consists of Te-Ga-Ga-Te tetra layers (TLs), with only two-thirds of Ga-Ga bonds lying perpendicular to the layer and the rest belonging to the horizontal direction. Such a complex structure promises low lattice thermal conductivity - a key advantage for achieving high TE performance. Further, the presence of atomically thin layers causes two-dimensional electronic transport induced by the quantum confinement effect together with enhanced phonon scattering at the interface. On the other hand, the electronic band structure of GaTe has a coexistence of flat and dispersive valence bands, which are incredibly beneficial for obtaining a large Seebeck coefficient and good electrical conductivity, respectively. Moreover, existing theoretical studies also predicted an unexpecting potential for GaTe-based TE materials. Thus, it is highly desired to explore the TE performance of GaTe-based materials. In fact, the pristine GaTe exhibits the low electrical conductivity due to the intrinsically low carrier concentration of ~10^{15} cm^{-3}. To achieving high performance, it is required to increase the carrier concentration of GaTe close to the optimal value, normally around 10^{19}-10^{21} cm^{-3}, depending on materials. To obtain this objective, we utilized bismuth (Bi) doping to enhance the TE performance of GaTe. In this thesis, we successfully prepared high-quality pristine GaTe and Bi-doped single crystals in a large size using a simple and effective "growth-from-the-melt" method, namely temperature gradient technique. As expected, Bi doping promoted to simultaneously increase

the hole concentration and mobility up to 1.63×10^{17} cm^{-3} and 68.25 cm^{2} V^{-1} s^{-1}, respectively, for BGT-4 samples. Our findings indicate the possibility of Bi doping in controlling the carrier concentration to increase the electrical and thermal properties of GaTe.

From the practical point-of-view, thermal stability on structural and thermoelectric characteristics is an essential inherent property from a practical standpoint. Good thermal stability helps ensure the long-term endurance, reliability, and repeatability of high-temperature responsive devices. Good thermal stability helps guarantee the long-term endurance, repeatability, and reliability of high-temperature responsive devices. Therefore, we systematically attempted to explore the structural thermal stability of GaTe single crystals in various atmospheres at temperatures ranging from 300 to 1173 K. Furthermore, we also studied the influences of annealing temperature on structural properties using photoluminescence and Raman spectroscopy. Our results indicate that GaTe is thermally stable up to 700 K in Ar and even higher up to 935 K in N_2 atmosphere due to the protective role of N_2 adsorbed layers on GaTe surface at high temperatures. The physical adsorption of N_2 molecules is originated from the weak electrostatic forces between quadrupole moments of N_2 molecules and surface Te atoms in GaTe material. Moreover, heat treatment considerably increases Moreover, heat treatment considerably increases the crystalline quality of GaTe with the optimal annealing temperature of 673 K.

Table of Contents

List of Figures

List of Tables

Chapter 1. Introduction

1.1. Importance of Thermoelectrics

Nowadays, the increasing population and economic growth require extensively increasing world energy consumption. **Figure 1.1** shows the annual global energy consumption by source reported the United States (U.S.) energy information administration (EIA) in 1990 - 2040. Clearly, global energy consumption will increase by approximately 50% between 1990 and 2040. Most of this growth is dominantly contributed from the developing countries, including China and India, where energy demand is driven by strong economic growth. By 2040, fossil fuels continue to dominate with an increase of 1.9 and 0.6% per year for natural gas and coal, respectively. Whereas the nuclear power and renewable energy increase by an average 2.6% per year through 2040, however, these energy sources still provide less 15% of the total world energy consumption.

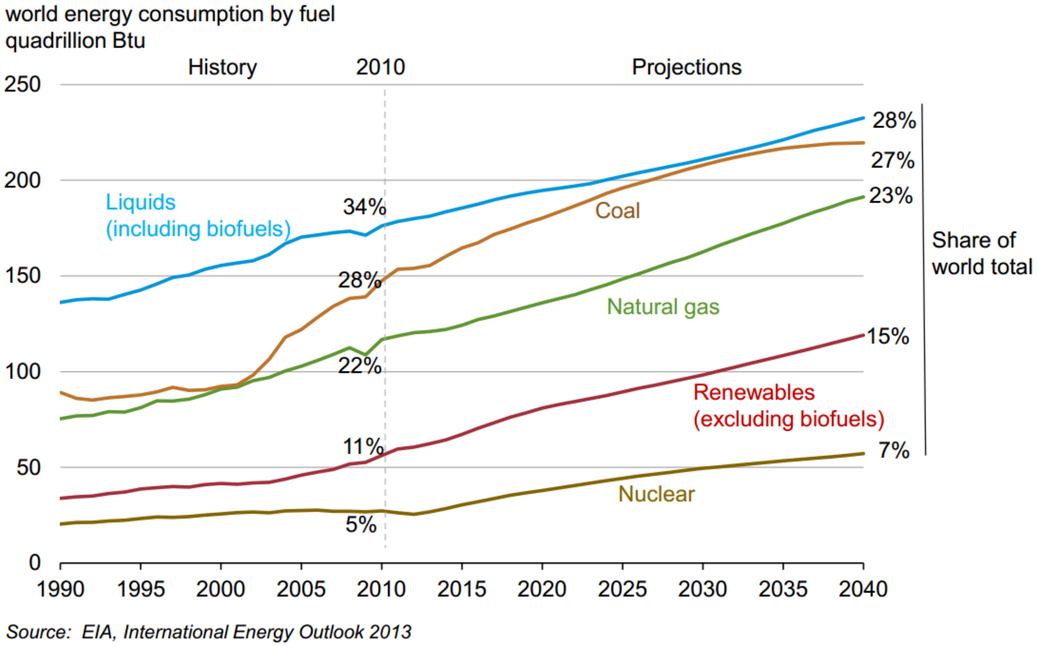

Source: *EIA, International Energy Outlook 2013*

Figure 1.1: The US energy information administration's (EIA) annual global energy consumption by source in 1990 - 2040.

In fact, the burning of fossil fuels in living and production activities releases large greenhouse gases, such as carbon dioxide (CO_2), methane (CH_4), and nitrous oxide (N_2O). **Figure 1.2** shows the contribution of various fuel energy sources to CO_2 emissions in the U.S. in 2020. Obviously, petroleum-related CO_2 emissions accounted for 45%, while natural gas and coal are the source of 36 and 19%, respectively, of total annual CO_2 emissions.

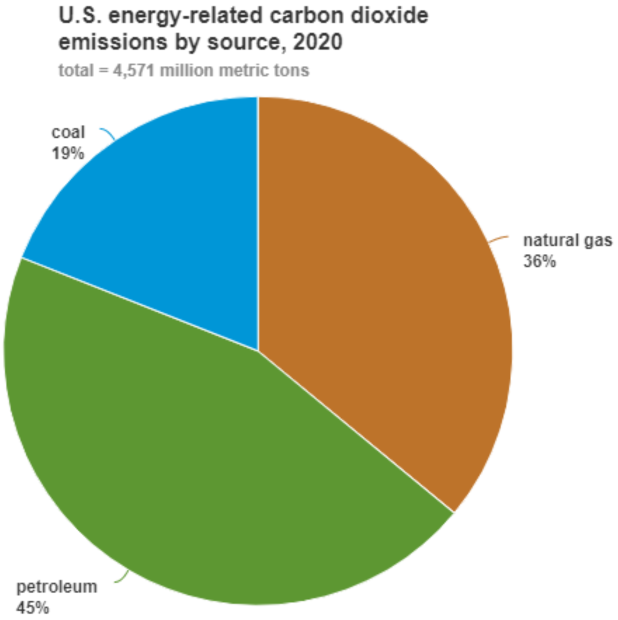

Figure 1.2: United State energy-related CO_2 emissions by source in 2020.

This release of greenhouse gases may be a primary contributing factor in global warming and climate change, leading to increasingly serious risks for ecosystems, human health, and the economy. In addition, fossil fuel resources will be rapidly exhausted in the next few decades. According to the BP Statistical Review of World Energy 2016, oil and natural gas will be depleted over the next 50 years, while the world only has 114 years of coal reserves left at current consumption rates (**Figure 1.3**). Thus, it is essential for developing clean and renewable energy sources, e.g., solar, wind, hydrothermal, and nuclear, besides the existing traditional ones.

Furthermore, it is estimated that more than 60% of energy input is mainly lost under the waste heat during the combustion and heat transfer process in industrial, transportation, and living activities. As shown in **Table 1**, losses in conventional power generators, transport systems, and motor systems can as be high as 45 to 90%, resulting low energy efficiency. Hence, thermoelectric (TE) technology has been proposed to become a powerful solution for waste heat recovery as well as a renewable energy source.

1.2.An Overview of Thermoelectrics

Currently, TE technology is emerging as a promising alternative energy source that could solve the above energy and global warming crises. TE modules, including TE power generators (TEGs) and TE coolers (TECs), enable directly converting thermal energy into electrical energy and vice versa[1]. TEGs are working based on the Seebeck effect, which discovered by German scientist Thomas Johann Seebeck in 1821. Whereas TECs operate according to a converse phenomenon of the Seebeck effect, called the Peltier effect, which was founded in 1834 by French physicist Jean Peltier. In comparison, TE modules offer many advantages of high reliability, no mechanical moving parts, compact in size, no noise, easy scalability, and lightweight[1]. In addition, the abundant wasted thermal energy can come from numerous sources, such as factories, electricity generators, vehicles, engines, and even the human body, with a wide released temperature range of 300 – 1000 K. As a result, TE modules have been considered as promising candidates for resolving energy issues in an environmental-sustainable viewpoint.

Table 1: Loss factors for selected equipment.

Energy system	***Percent Energy Lost***
Steam systems	Boiler – 20% Steam pipes and traps – 20% Steam delivery/heat exchangers – 15%
Power generation	Combined heat and power – 24% Conventional power – 45%
Energy distribution	Fuel and electricity distribution lines and pipes – 3%
Energy conversion	Process heaters – 15% Cooling systems – 10% Onsite transport systems – 50% Electrolytic cells – 15% Other – 10%
Motor systems	Pumps – 40% Fans – 40% Compressed air – 80% Refrigeration – 5% Materials handling – 5% Materials processing – 90% Motor windings – 5%

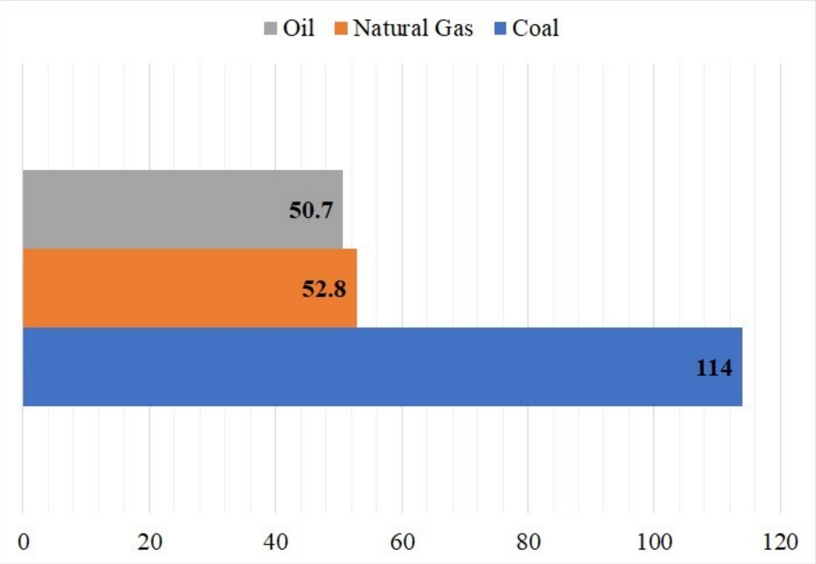

Figure 1.3: Number of years of fossil fuel left based on known reserves and annual production levels in 2015.

Figure 1.4 shows a schematic diagram illustrating components and arrangement of a practical TE module, which generally consists of n- and p-type semiconducting pairs that are thermally connected in parallel and electrically in series. These n-p pairs are joined by conductive plates and then sandwiched between two ceramic substrates. In fact, a typical TE module is composed of few hundreds of n-p pairs to create large output power. However, higher number of n-p thermoelements will also proportionally increase the total internal resistance as expressed as:

$$R_{TEG} = N\left(\frac{\rho_A L_A}{S_A} + \frac{\rho_B L_B}{S_B} + 2\frac{\rho_C L_C}{S_C}\right) \qquad (1-1)$$

where ρ_A, ρ_B, and ρ_C are the electrical resistivity of materials A, B, and contacted conductive plates, respectively. L_A and L_B are thermoelement lengths and L_C is the contact length. S_A, S_B, and S_C are, respectively, cross-sectional areas of the A and B thermoelements and contacts. Clearly, the internal resistance depends on both intrinsic material characteristics and extrinsic properties such as geometric dimensions. In general, the high internal resistance of thermoelectric modules causes a considerable Joule heating ($Q_J = I^2 R_{TEG}$), which degrades device performance. When the external electric load in the circuit is nearly equal to the internal resistance, the maximum output power is obtained with a peak current (I_{max}) traveling through TE modules.

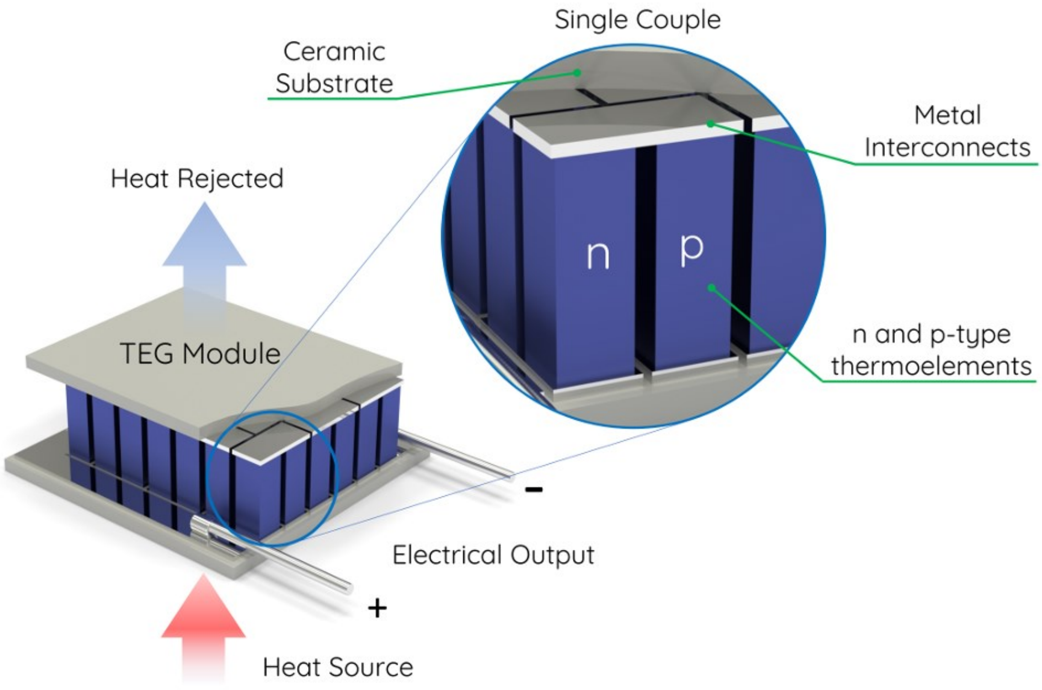

Figure 1.4: Schematic diagram of a typical thermoelectric module.

There are three major impediments to the widespread use of TE modules[2]: (i) the low conversion efficiency and low chemical stability of TE elements, (ii) the toxicity and criticality of elements used in TE materials, (iii) the mechanical rigidity of TE modules. Up to date, the commercial devices assembled from Bi_2Te_3-based materials operate below 550 K with a typically low conversion efficiency of about 3-6%[3], limiting the application range of TE modules. On the other hand, commercial Bi_2Se_3-based modules have demonstrated a significant performance degradation under thermal cycling tests. After 6000 repeated thermal cycles ranging from 300 to 430, the maximum output power is decreased by 11%. Mechanical damage, including voids, pores, and cracks, was observed at the interface between the Bi_2Te_3 legs and Cu contacts[4]. This is originated from the low chemical and thermal stability of Bi_2Te_3

materials in long-term high-temperature operation. PbTe, a traditional TE material for immediate temperatures, showed poor mechanical properties with relatively low biaxial fracture strength, leading to microcracking during thermal cycling. Furthermore, Pb is a highly toxic element with harmful effects on human health, so lead-free devices with high performance are highly demanded. Over the few past decades, a variety of efforts has been carried out to create new high-performance TE materials with desirable characteristics.

1.3. Thermoelectric Conversion Efficiency

The efficiency (η) of a TE module relies directly on the temperature gradient (ΔT) and the average dimensionless figure-of-merit (zT_{ave}) of a given material, as describes below in **Equation (1-2)**[1,5]:

$$\eta = \frac{\Delta T}{T_{hot}} \frac{\sqrt{1 + zT_{ave}} - 1}{\sqrt{1 + zT_{ave}} + \frac{T_{cold}}{T_{hot}}} \qquad (1-2)$$

where T_{hot}, T_{cold} are the hot- and cold-side temperatures, respectively. For a given temperature difference, it is clearly seen that a higher zT_{ave} will produce the higher conversion efficiency (**Figure 1.5**). The efficiencies of current state-of-art TE devices are approximately 5-20% for zT_{ave} values lower than 2. By increasing zT_{ave} up to the factor of 3, the predicted efficiency can reach 25% at ΔT = 400 K, comparable to that of traditional heat engines[1]. However, the conversion efficiency is a fraction of the Carnot efficiency even though zT_{ave} approaches infinity. Note that the dimensionless figure-of-merit zT is temperature-dependent, thus high zT values throughout a wide temperature range are significantly necessary for achieving large zT_{ave}. Furthermore, the device's figure-of-merit zT can differ significantly from that of the material for a variety of reasons, including substantial temperature variations in zT and poor TE self-compatibility across the temperature range and between the legs.

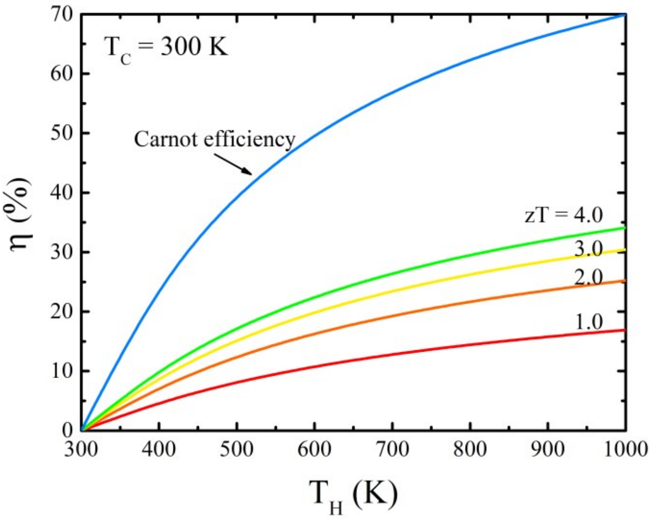

Figure 1.5: Conversion efficiency of TE material with changing temperature difference and zT, assuming that the cold side temperature is 300 K.

1.4.Thermoelectric Effect

Thermoelectric modules can be divided into two parts: one is thermoelectric generators[6,7] (TEGs) converting thermal energy into electrical energy via the Seebeck effect, and another is thermoelectric coolers[8] (TECs) via the Peltier effect.

1.4.1. Seebeck Effect

Historically, in 1821, the German scientist Thomas Johann Seebeck proposed a phenomenon, namely Seebeck effect, which can be simply schematized by **Figure 1.6**, where an applied temperature difference drives the charge carriers (holes and/or electrons) to diffuse from the hot side to cold side. This diffusion creates a current flow through the closed circuit, inducing a potential difference V.

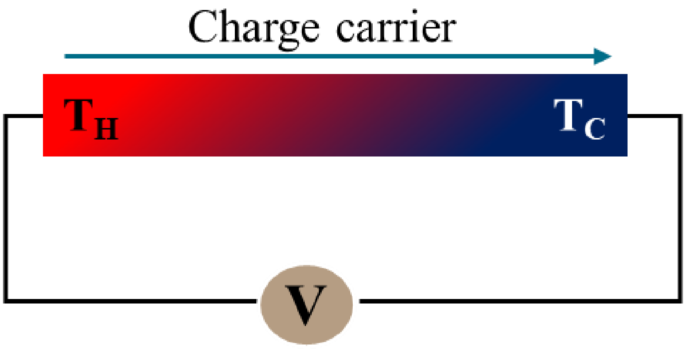

Figure 1.6: Schematic diagram illustrating the Seebeck effect.

This effect is quantified by the Seebeck coefficient (also called thermopower) as the following **Equation (1-3)**

$$S = \frac{V}{\Delta \mathrm{T}} \tag{1-3}$$

where V is the induced voltage in response to an applied temperature gradient between the hot and cold ends ΔT.

1.4.2. Peltier Effect

In 1834, Jean Peltier observed a reverse phenomenon of the Seebeck effect, namely the Peltier effect. As shown in **Figure 1.7**, a potential difference applied across two coupled dissimilar conductors causes a temperature difference between the junctions.

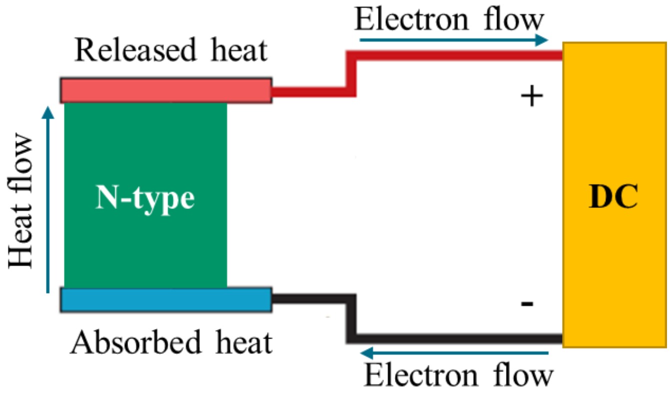

Figure 1.7: Schematic diagram illustrating the Peltier effect.

The Peltier heat generated at the junction per unit time is defined by **Equation (1-4)**:

$$\frac{dQ}{dt} = I\pi_{ab} \qquad (1-4)$$

where I is the applied electric current and π_{ab} is the Peltier coefficient.

1.4.3. Thomson Effect

The Thomson effect is originally proposed by William Thomson (also known as Lord Kelvin) in 1851. It describes the heat absorption or releases when the electric current flows across a single conductor carrying a temperature gradient. As shown in **Figure 1.8**, if the temperature gradient has a direction opposite to the applied current, the heat is released and vice versa.

The Thomson heat (Q) is proportional to both the electric current (I) and temperature gradient (ΔT) as describes by **Equation (1-5)**:

$$Q = \beta I \Delta T \qquad (1-5)$$

where β is the Thomson coefficient. Thus, in an n-type semiconductor, the Thomson coefficient is always negative, while in a p-type semiconductor, it is always positive. The

Thomson heat is reversible between heat and electricity, which is different from the Joule heating produced by an electric current through a conductor of resistance.

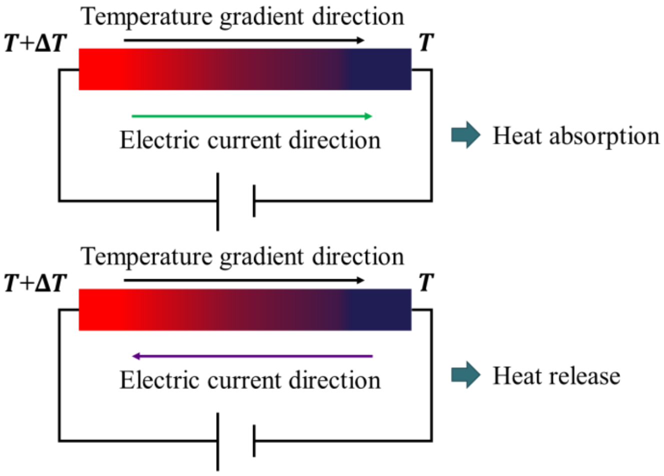

Figure 1.8: Schematic diagram illustrating the Thomson effect.

1.4.4. Complex Interdependence of Thermoelectric Parameters

As mentioned above, the thermoelectric efficiency of a TE material is expressed by the dimensionless figure-of-merit zT, which is determined by three parameters as following **Equation (1-6)**:

$$zT = \frac{S^2\sigma}{k}T = \frac{S^2\sigma}{k_e + k_l}T \qquad (1-6)$$

where S, σ, k, k_e, k_l, and T are the Seebeck coefficient, electrical conductivity, total thermal conductivity, electronic thermal conductivity, lattice thermal conductivity, and absolute temperature, respectively[9]. An ideal thermoelectric material should satisfy the following criteria: a large Seebeck coefficient, high electrical conductivity, and low thermal conductivity. Low thermal conductivity is to maintain a considerable temperature difference between two ends of the material. High electrical conductivity helps to reduce the internal resistance, thereby reducing the Joule effect. Whereas a large Seebeck coefficient is required to obtain a high voltage induced by the temperature difference. However, it is challenging to satisfy simultaneously these key parameters due to their complex interdependence.

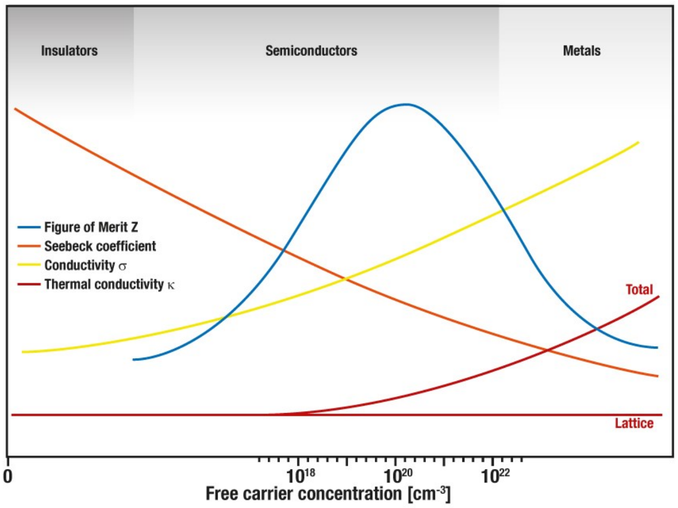

Figure 1.9: The Seebeck coefficient, electrical conductivity, total thermal conductivity, and figure-of-merit as a function of carrier concentration.

As shown in **Figure 1.9**, metals have very high electrical conductivity but also very high thermal conductivity. Whereas insulators exhibit opposite behaviors, having very low thermal conductivity but also ultra-low electrical conductivity. Thus, high-performance thermoelectric materials should be in the heavily doped semiconductor region with carrier concentration on the order of 10^{19} to 10^{21} cm^{-3}.[10]

1.5. Research Objectives

Gallium telluride (GaTe), a member of group IIIA chalcogenides, crystalizes in a low-symmetry monoclinic layered structure. Many recent theoretical studies have suggested GaTe as a good candidate for thermoelectric application. The overall objective of this doctoral work is to systematically investigate the potential for thermoelectric application of GaTe-based systems. In this thesis, we have proposed three essential objects as following:

(1) To prepare high-crystallinity GaTe single crystals in large-size.

We used the “growth-from-the-melt” method, namely “temperature gradient technique”, to successfully fabricate the large-size high-quality GaTe single crystals. **Figure 1.10** shows the schematic diagram of the temperature gradient technique. In this technique, the crystalline formation originated from a crystal seed formed by the conical-shaped quartz tube bottoms. Interestingly, the cooling rate across the melting point plays a prerequisite role in the single crystalline formation. Our findings indicate that the slow cooling rate of ~0.5 - 1 K h^{-1} is best to achieve high-quality GaTe single crystals in large size.

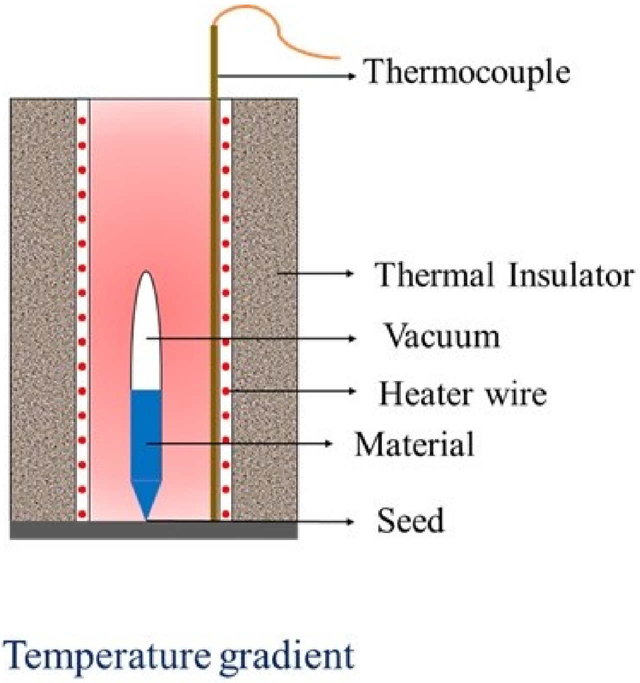

Figure 1.10: Schematic diagram of the temperature gradient technique.

(2) To probe the intrinsic thermal stability of GaTe single crystals.

Thermal stability is an important intrinsic characteristic for thermoelectric materials, which represents the ability to resist the decomposition and/or transformation on prolonged exposure to elevated temperatures. To probe the operating temperature range, we performed the thermogravimetric analysis (TGA) and differential scanning calorimetry (DSC) measurements under inert atmospheres (N_2 and Ar) in the temperature range of 300 – 1173 K. Furthermore, we also characterized the influences of thermal treatment on the GaTe crystal structure using Raman spectroscopy and photoluminescence (PL) analysis.

(3) To enhance thermoelectric performance of GaTe single crystals.

We proposed the doping ability of bismuth (Bi) to tune the carrier concentration, thereby improving their thermoelectric performance. Remarkably, the carrier concentration and mobility are significantly increased compared with the pristine GaTe, resulting in higher thermoelectric performance.

1.6. Thesis Organization

This doctoral thesis is organized as follow:

Chapter 1 presents a brief background of the importance, basic principles of thermoelectric technology, and the challenge to achieve high thermoelectric performance. Chapter 2 reviews the strategies for improving the performance of thermoelectric materials. The literature review on the GaTe compound is also presented. Chapter 3 describes the experimental techniques to fabricate and investigate the crystal structure, electrical thermal transport properties, and thermal stability of GaTe-based single crystals.

For chapter 4, we reveal an investigation of thermal stability on crystal structure in various atmospheres for GaTe single crystals. We discovered different responses of GaTe material as undergoing the heating in different gas atmospheres. The underlying mechanism also clarified in this chapter. Chapter 5 demonstrates the effect of Bi doping in the crystal structure and thermoelectric properties of GaTe single crystals. We also provide the doping mechanism and understanding of correlations of thermoelectric parameters in Bi-doped GaTe material. Chapter 6 summarizes the conclusions and provides outlooks for further research work related to the GaTe-based thermoelectric materials.

Chapter 2. Literature Review

As mentioned in the chapter 1, a material with high thermoelectric performance (zT) needs to have a large Seebeck coefficient (S), a high electrical conductivity (σ), and a reduced thermal conductivity (k). Thus, the major activities in thermoelectric materials would be focused on increasing the S and σ as well as suppressing the k.

2.1. Strategies for Improving Electrical Conductivity

Electrical conductivity is a fundamental quantity that measures the carrying ability of an electric current in a conductor. The relationship between electrical conductivity (σ) and carrier concentration (n) can be defined as **Equation (2-1)**:

$$\sigma = ne\mu \qquad (2-1)$$

where μ denotes the carrier mobility and e is the electric charge (e = 1.6 × 10^{-19} C)[11]. Thus, the σ could be improved by increasing these two parameters separately or simultaneously.

2.1.1. Optimizing Carrier Concentration

Generally, there are two different ways to alter the carrier concentration, *i.e.*, extrinsic doping and tuning intrinsic defects.

Extrinsic doping (**Figure 2.1**) is the intentional introduction of impurities into an intrinsic material enabling to tune the charge carriers. By varying the type of dopants (acceptors/donors), the major charge carriers (holes/electrons) could be easily switched. However, although the idea is likely simple, choosing a suitable dopant is not easy work. For the optimum effect, the selection of ionic dopant must meet the following criteria: small cation radii, large anion radii, less sensitivity to ambient moisture, nontoxicity, and good solubility.

The optimum carrier concentration cannot sometimes be achieved due to the solubility limit and the doping efficiency of the dopants. In fact, the solubility strongly depends on the formation of defects containing the dopants. As shown in **Equation (2-2)**, the formation energy depends on the chemical potentials of the host elements and relevant impurity atoms[12].

$$DH^{(D,q)} = qE_F + n_D(\mu_D - \mu_H) + DE_b \qquad (2-2)$$

where μ_D and μ_H are the chemical potentials of the dopant and hosts, E_F is the Fermi energy, n_D is the number of dopants, $DE_b = E$ (host + defect) - E (host) is the excess energy of the local chemical bonds around the dopant, and E is the total energy. In addition, the solubility limit also depends on whether the materials are cation-rich or anion-rich. Specifically, anion-substituting dopants would be more soluble under host cation-rich growth conditions, whereas dopants would be easier to substitute the cation sites under anion-rich compounds[12,13]. Therefore, it is essential to investigate the high-solubility dopants for altering the carrier concentration of host materials.

Tuning intrinsic defects, including vacancies, interstitials, and anti-sites (**Figure 2.1**), is a successful way to optimize the carrier concentration. Typically, intrinsic point defects are very sensitive to the composition and can be manipulated by changing growth conditions and/or extrinsic doping. For example, the intrinsic Te_{Bi} anti-site defects are responsible for the n-type conducting Bi_2Te_3 in the Te-rich condition, while Bi_{Te} anti-site defects are dominant in p-type Bi_2Te_3 under Bi-rich growth condition[14].

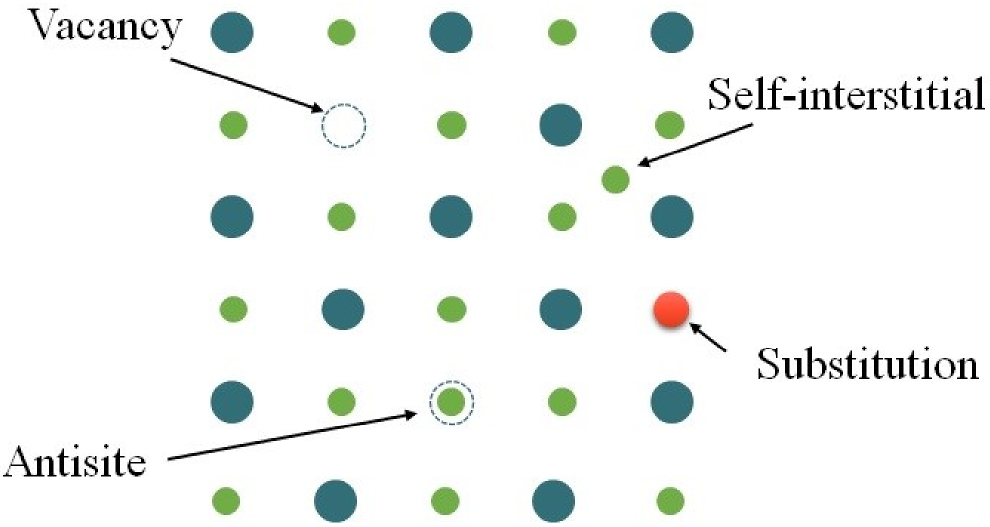

Figure 2.1: Schematic diagram illustration of common point defects.

2.1.2. Increase Carrier Mobility

Carrier mobility (μ) is typically defined by the following **Equation (2-3)**:

$$\mu = \frac{n}{E} \qquad (2-3)$$

where n and E are the drift velocity and applied electric field, respectively. This quantity measures how quickly a charge carrier can move through a material under an applied electric field.

Based on a simple parabolic band assumption, the carrier mobility can be expressed by **Equation (2-4)**:

$$\mu = \frac{e}{m^*}\tau \qquad (2-4)$$

where τ and m^* are the average scattering time and effective mass, respectively[15]. Thus, the carrier mobility can be improved either by increasing the scattering time or by decreasing the effective mass.

The scattering time is related to the scattering mechanisms, such as ionized impurity scattering, lattice (phonon) scattering, alloy scattering, surface scattering, electron-electron scattering, *etc*. **Figure 2.2** illustrates the relationship between mobility and two predominant carrier scattering mechanisms in semiconductors. In doped semiconductors, charge carriers will be deflected as approaching the ionized impurity due to Coulombic forces. Below 300 K, carriers move more slowly, so carriers have more time to interact with ionized impurities (crystal defects), leading decreasing mobility with decreasing temperature. At high temperatures, phonon scattering plays a dominant contribution due to increased lattice vibration. Thus, the carrier mobility significantly decreases in the high temperature range (>300 K). Note that scattering centers originated from point defects (vacancies, interstitials, anti-sties, substitutions), grain boundaries, lattice dislocations, *etc.* By compensating point defects and increasing the grain sizes, the carrier mobility could be significantly enhanced.

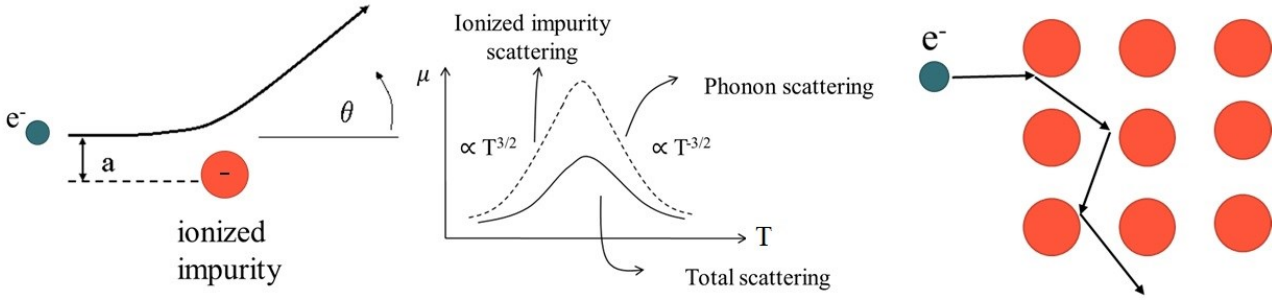

Figure 2.2: Relationship between mobility and carrier scattering mechanisms.

Furthermore, modulation doping is a well-developed technique that is widely used in two-dimensional materials for improving carrier mobility[16]. As shown in **Figure 2.3**, modulation doping is related to the nonuniform distributions of dopants in the pristine material. Consequently, the modulation-doped sample consists of two phases, *i.e.*, pristine phase and heavily doped phase. The pristine phase exhibits lower carrier concentration but higher carrier mobility, whereas the heavily doped phase shows higher carrier concentration but lower carrier concentration. The combination of these phases results in overall enhanced carrier mobility in comparison to uniformly doping. For instance, with Ba^{2+} uniformly doping, the room-temperature carrier concentration significantly increases from ~1.1 × 10^{18} cm^{-3} for pristine BiCuSeO to ~1.2 × 10^{21} cm^{-3} for the uniformly doped $Bi_{0.875}Ba_{0.125}CuSeO$. Owing to the enhanced scattering induced by impurities, the carrier mobility dramatically decreases from 22 cm^2 V^{-1} s^{-1} for undoped BiCuSeO to 2.1 cm^2 V^{-1} s^{-1} for the uniformly doped $Bi_{0.875}Ba_{0.125}CuSeO$. However, the modulation-doped $Bi_{0.875}Ba_{0.125}CuSeO$ shows carrier mobility of ~4.1 cm^2 V^{-1} s^{-1}, which is almost twice as high as that of the uniformly doped $Bi_{0.875}Ba_{0.125}CuSeO$ with a similar carrier concentration[16].

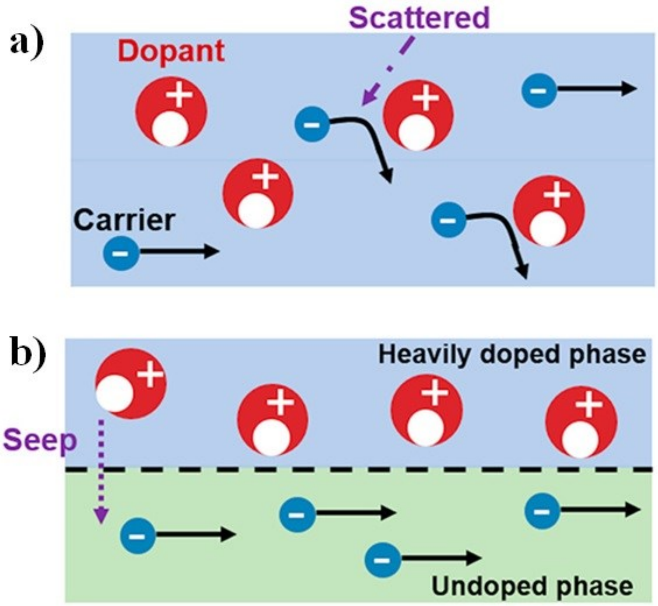

Figure 2.3: Comparison of (a) uniform doping and (b) modulation doping.

As mentioned above, reducing the effective mass is also an effective way to increase carrier mobility. Basically, the effective mass (m^*) is assigned to a mass of particles (electrons or holes) traveling in a crystal under the action of periodic potential induced by the lattice atoms. In the band approximation, the effective mass is derived from **Equation (2-5)**:

$$\left(\frac{1}{m^*}\right)_{\mu n} = \frac{1}{\hbar^2}\left[\frac{\partial^2 E(k,0)}{\partial k_\mu \partial k_n}\right]_{k=k_m} \qquad (2-5)$$

where $E(k,0)$ is the band energy dispersion and k_m are the wave vectors of band minima or maxima. Clearly, bands of large curvature (dispersive bands) correspond to small effective masses, while bands of small curvature (flat bands) correspond to heavy effective masses (**Figure 2.4**). Therefore, band engineering is an aggressive strategy to modify band dispersion, consequently tuning effective mass and carrier mobility of material.

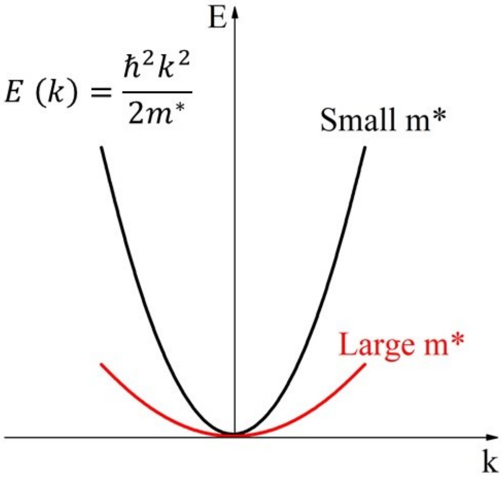

Figure 2.4: Relationship between effective mass and band dispersion.

2.2. Increase Seebeck Coefficient

Because the thermoelectric figure-of-merit zT scales with S^2, improvement in the Seebeck coefficient seems more efficient than enhancing the electrical conductivity in achieving high zT. Usually, S is expressed by the Pisarenko relationship as the following **Equation (2-6)**:

$$S = \frac{8\pi^2 k_B^2 T}{3eh^2} m^* \left(\frac{\pi}{3n}\right)^{\frac{2}{3}} \qquad (2-6)$$

where n and m^* are the carrier concentration and effective mass, respectively. It can be clearly seen that a high effective mass m^* is beneficial for a high Seeck coefficient. Large m^* can be achieved by either a high band degeneracy (N_v) or a flat band.

2.2.1. Band Flattening

Band flattening, which can be occurred through doping or alloying, is the common way to increase the effective mass. For example, La-doped PbTe samples demonstrated higher Seebeck coefficient values compared to I-doped samples with similar carrier concentrations. This corresponds to a 20% higher effective mass in La-doped samples[17]. Theoretical calculations revealed that the conduction band at the L-point can be flattened by the hybridization between La f-states and Pb p-states, resulting in an increased effective mass in La-doped PbTe[18]. For another typical example, $AgSbTe_2$ alloying can regulate the electronic structures of SnSe, leading to the improvement of effective mass as well as the Seebeck coefficient[19].

2.2.2. Band Convergence

The band convergence is achieved when different bands with different energies are engineered to have the same energy. Depending on the materials and band positions in the Brillouin zone, the band energy can vary with the chemical composition and temperature (**Figure 2.5**). PbTe is well known to have a valence band at L-point and another band at Σ-point 0.18 eV below at 0 K[20,21]. With increasing temperature, the energetic separation of two valence bands gradually decreases, reaching the same energy at 450 K[21]. Additionally, the electronic band structure of PbTe can be manipulated through alloying[22] and/or doping. This approach has also demonstrated in various thermoelectric materials, including SnTe[23], GeTe[24], Mg_3Sb_2[25,26], *etc.*

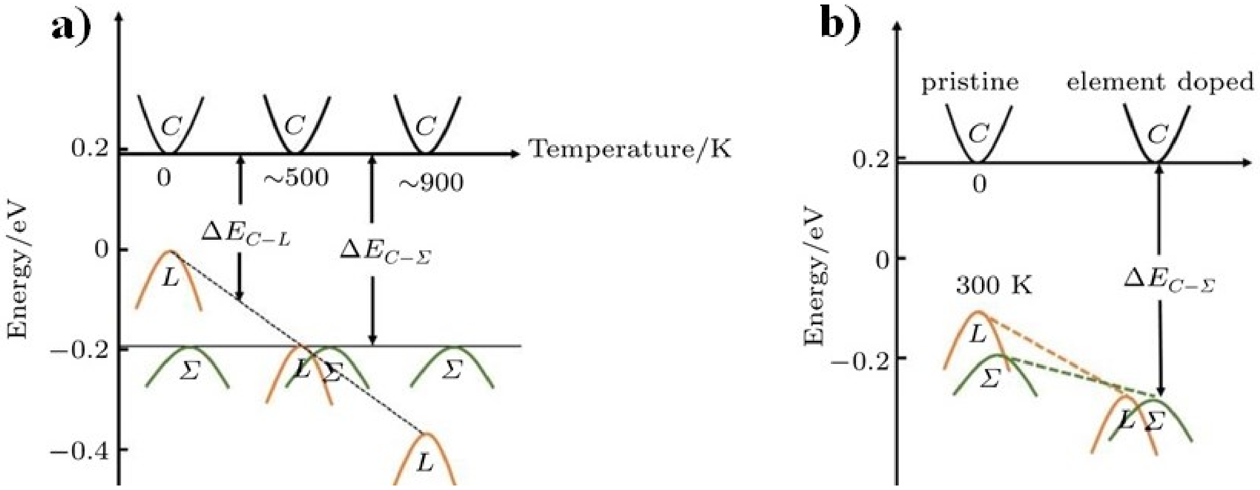

Figure 2.5: (a) Scheme of temperature-induced band convergence in PbTe. (b) Scheme of dopants-induced band convergence in doped PbTe.

2.3. Suppressing Thermal Conductivity

Generally, the total thermal conductivity (κ) mainly consists of three parts, including the electronic thermal conductivity (k_e), lattice thermal conductivity (k_l), and bipolar thermal conductivity (k_b), as described by **Equation (2-7)**.

$$k = k_e + k_l + k_b \qquad (2-7)$$

The electronic thermal conductivity k_e is defined by the Wiedemann-Franz-Lorenz law, $k_e = L\sigma T$, where L is the Lorenz parameter, which does not vary much from material to material, remaining in the range of 1.6 to 2.5 × 10^{-8} V^2 K^{-2}. Obviously, the electronic thermal conductivity does not play a dominant impact on total thermal conductivity. Hence, to obtain high thermoelectric performance, a low lattice thermal conductivity and low bipolar thermal conductivity should be achieved. Note that the bipolar contribution is important only when $\sigma_n \gg \sigma_p$, here σ_n and σ_p denote the electrical conductivity induced by electrons and holes, respectively. In other words, the bipolar thermal conductivity is only significant in narrow semiconductors and high temperatures. Therefore, suppressing lattice thermal conductivity is essential to increase zT. There are two main approaches to achieve low lattice thermal conductivity, *i.e.*, enhancing phonon scattering through introducing the scattering centers and developing new materials with intrinsically low thermal conductivity.

2.3.1. Enhancing Phonon Scattering

Basically, the lattice thermal conductivity k_l arises from contributions by phonons with differential frequencies (ω) ranging from the short-to-long wavelength. Thus, to reduce thermal conductivity, ideally, one attempts to suppress the propagation of phonons by introducing the scattering centers.

For PbTe-based systems, short-wavelength phonons contribute 25% of the lattice thermal conductivity, while more than 50% of the lattice thermal conductivity is offered via the medium wavelength, and the rest is donated from long-wavelength phonons[27]. Thus, for effectively scattering these different phonons as well as reducing the lattice thermal conductivity, the phonon scattering at atomic-scale point defects, nanoscale inclusions, and mesoscale grain boundaries were utilized to reduce the propagation of short-, mid-, and long-wavelength phonons, respectively (**Figure 2.6**).

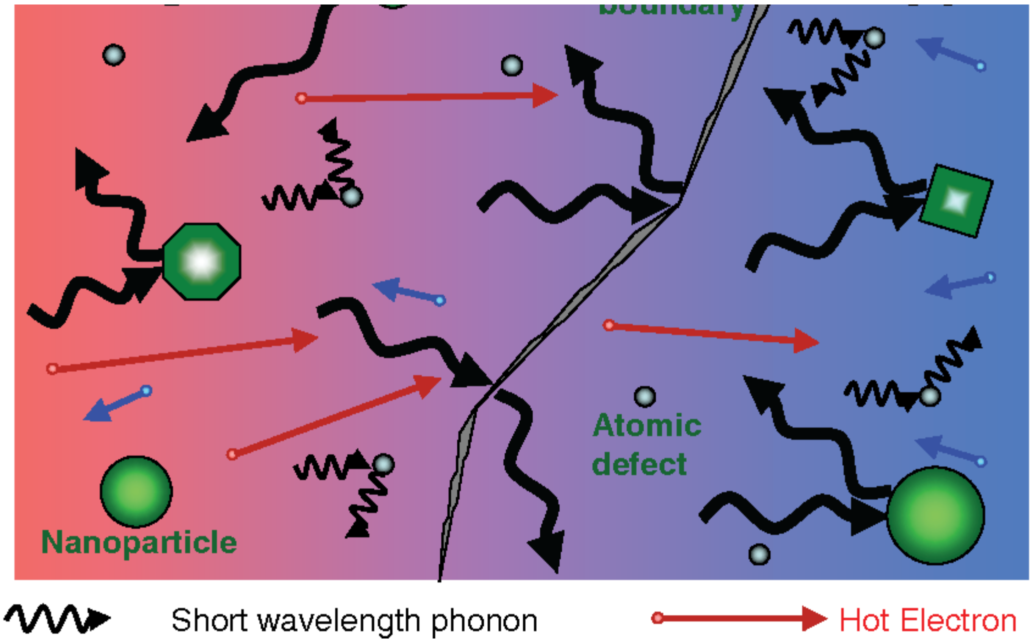

Figure 2.6: Schematic diagram illustrating phonon scattering mechanisms in thermoelectric materials.

2.3.2. Developing New Materials with Intrinsically Low Thermal Conductivity

In the past decades, numerous novel thermoelectric materials with intrinsically low lattice thermal conductivity, for instance, SnSe[28], BiCuSeO[29], MgAgSb[30], Cu_2Se[31], *etc.*, have been developed. The underlying mechanisms in intrinsically low thermal conductivity of such materials would be discussed in this section.

Above the Debye temperature (θ_D), if the phonon-phonon Umklapp scattering dominates the phonon transport, the lattice thermal conductivity is expressed by **Equation (2-8)**:

$$k_l = A\frac{\bar{M}\theta_D^3\delta}{\gamma^2 N^{\frac{2}{3}} T} \qquad (2-8)$$

where $\bar{M}$, δ^3, N, γ are the average atomic mass, volume per atom, number of atoms in the primitive unit cell, and Grüneisen parameter characterizing the anharmonicity of materials, respectively. The formula indicates that the materials with intrinsically low k_l should have strong anharmonicity, low Debye temperature, complex primitive unit cell, and heavy constituent elements.

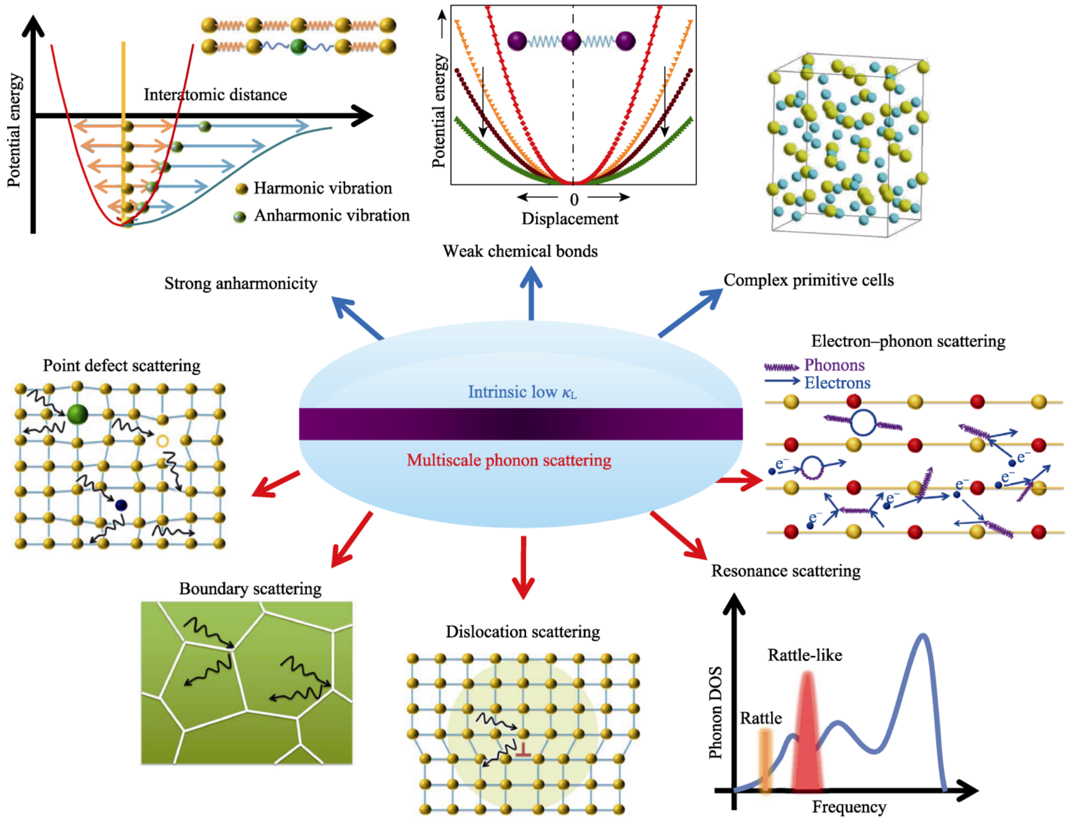

Figure 2.7: Several underlying mechanisms in intrinsically low thermal conductivity of typical thermoelectric materials.

Figure 2.8 illustrates the potential energy of harmonic and anharmonic oscillators as functions of the displacement x. Strong anharmonicity, which can be characterized by a large Grüneisen parameter γ, indicates strong phonon-phonon interactions, leading to low lattice thermal conductivity. Grüneisen parameter γ describes the change in the volume of a crystal lattice due to thermal vibration, as expressed by **Equation (2-9)**[32].

$$\gamma = \frac{\alpha K_T}{C_V \rho} \qquad (2-9)$$

Clearly, a large Grüneisen parameter requires a large thermal expansion coefficient (α), large bulk modulus (K_T), low specific heat (C_V), and low mass density (ρ). Note that the thermal expansion coefficient, bulk modulus, and specific heat are dependent on the bond strength and type between atoms. Specifically, materials with strong ionic/covalent bonds have low thermal expansion coefficients, high specific heats, and small bulk modulus. Thus, weaker chemical bonding is a crucial factor leading to strong anharmonicity as well as low lattice thermal conductivity in some thermoelectric systems, especially, layered materials[33].

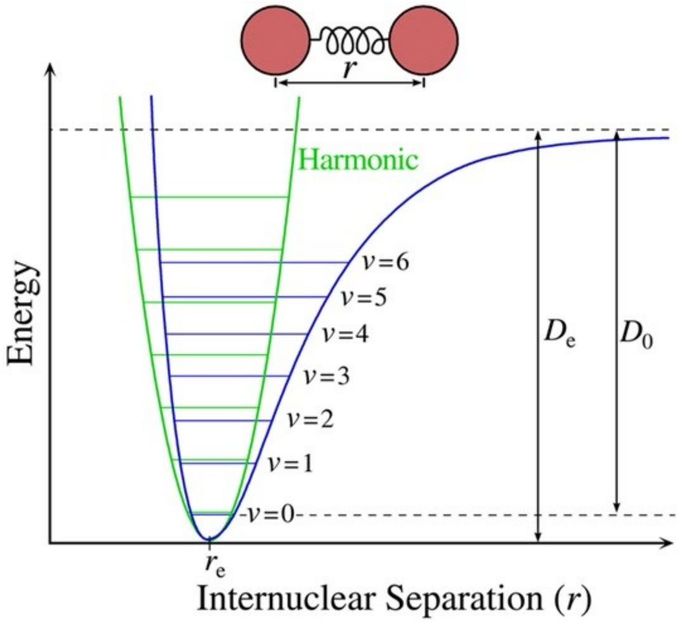

Figure 2.8: Schematic representation of the harmonic (green) and anharmonic (blue) oscillation for the potential energy of a diatomic molecule.

In addition, the complex crystal structure may lead to the existence of numerous optical phonons. The optical phonons usually have very low group velocity and contribute little to the thermal transport. The increased number of optical phonons with increasing number of atoms in a primitive unit cell N tends to lower the space and frequency of acoustic phonons, contributing to the k_l reduction.

Furthermore, materials composing of heavy constituent elements favor high thermoelectric performance because their heavy constituent elements could act as phonon rattlers to help suppress the lattice thermal conductivity effectively[34].

2.4. Gallium Telluride – Can Become New Potential Thermoelectric Materials?

2.4.1. Crystal Structure and Electronic Properties - An Overview

Gallium telluride (GaTe), a layered material, has attracted a lot of attention in recent years for solar cells, optoelectronics, and thermoelectric applications[35–37]. Bulk GaTe possesses a monoclinic crystal structure belonging to the $C2/m$ space group – analogous to the structure of GeAs[38,39]. Contrasting to the other members of the group III-VI chalcogenide family, GaTe has a low in-plane symmetric crystal structure with one-third of the Ga-Ga bond lying horizontally and the rest two-thirds perpendicular to the layer plane[40,41]. This difference causes a two-dimensional monoclinic structure of GaTe instead of a hexagonal structure such as GaSe and InSe. As represented in **Figure 2.9**, the layered crystal structure of GaTe consists of Te-Ga-Ga-Te tetra layers (TLs) formed by strong covalent bonds. Two adjacent TLs are weakly coupled via van der Waals interactions. The thickness of single-layer GaTe is around 7.47 Å preferentially stacking along $(\bar{2}10)$ direction with lattice constants $a = 17.40$ Å, $b = 4.08$ Å, and $c = 10.46$ Å, and $\beta = 104.50°$. Owing to such different bonding strength, GaTe reveals strong anisotropy on mechanical, thermal, and electrical properties along different crystallographic directions.

GaTe is a semiconductor with a direct band gap of 1.65-1.67 eV at room temperature and 1.78 eV at 0 K. **Figure 2.10** shows the calculated electronic band structure of GaTe material using density functional theory (DFT) reported by Brudnyi[42]. The energy position of the charge neutrality level (CNL) of GaTe is 0.72 eV at room temperature, indicating the persistent p-type conductivity in GaTe material. In addition, GaTe demonstrates a complex electronic band structure with 21 different valence bands in the range from -8 to 0 eV. The valence bands ranging from -8 to -4 eV are mainly composed of 4s states with a significant contribution of anion p states. The uppermost energy levels are predominantly formed by anion and cation p states with a small admixture of s orbitals. Furthermore, there is a co-existence of light (dispersive) and heavy (flat) topmost valence bands (VBs) at Z- and P-point, respectively, as shown in **Figure 2.10**. Such features are incredibly beneficial for reaching high thermoelectric performance.

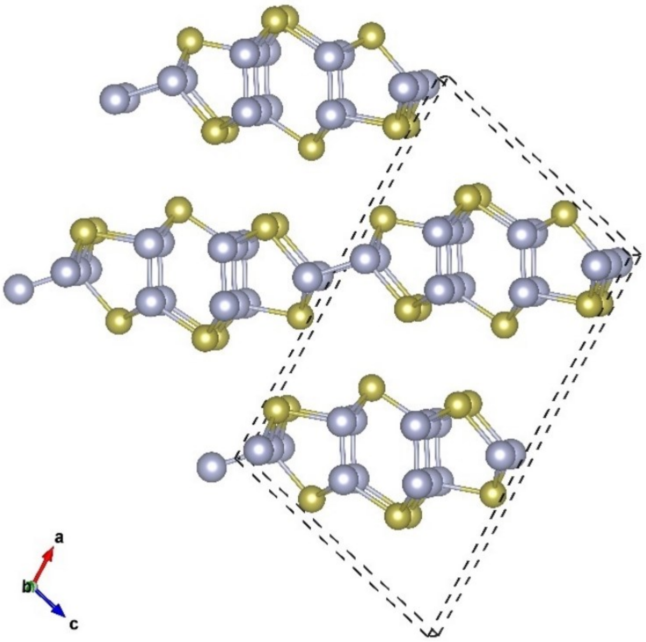

Figure 2.9: Monoclinic structure of GaTe. Yellow and violet solid spheres represents Te and Ga atoms, respectively.

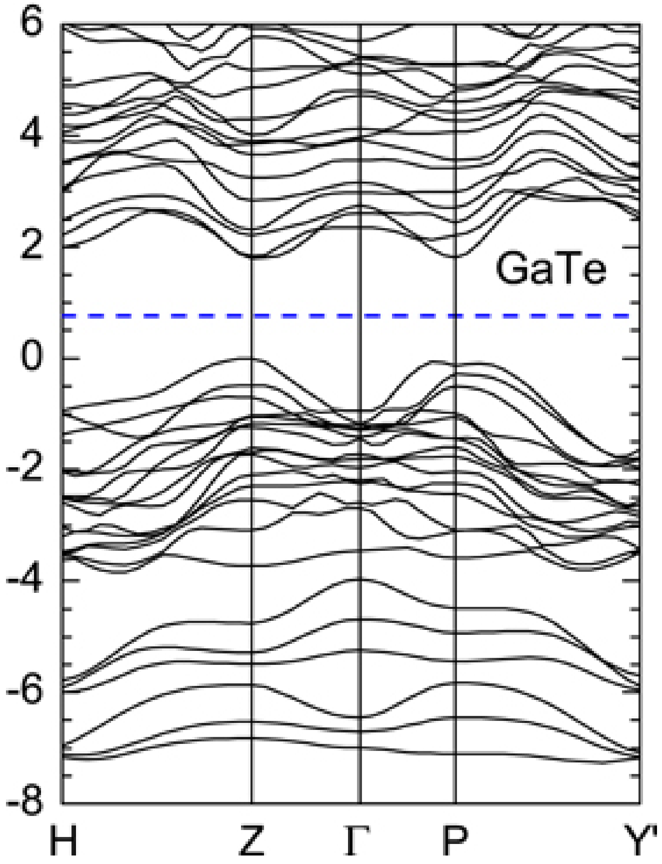

Figure 2.10: Calculated electronic band structure of GaTe compound using density functional theory (DFT). The dashed lines indicate the location of charge neutrality level (CNL) at low temperature.

2.4.2. Advantages for High Thermoelectric Performance

GaTe has been regarded as a good thermoelectric material due to the following advantages:

Anisotropic characteristics: Owing to the strong anisotropy in chemical bonding between in-plane and out-of-plane layers, GaTe would demonstrate the anisotropic properties with different crystallographic directions. By manipulating these anisotropic characteristics, it is effortless to tune individually the electrical and thermal properties for enhancing TE performance. This strategy has demonstrated effectiveness in many high ZT materials such as SnSe[43,44] and Bi_2Te_3.[45]

Layered crystal structure: GaTe promises thermal conductivity as low as analogous crystal structure materials such as GeAs[38] and As_2Se_3[46] due to strong phonon scattering at interlayer interfaces.

Coexistence of flat and dispersive valence bands: As mentioned above, band structure of GaTe coexists simultaneously dispersive and nearly flat valence bands at Z- and P-point, respectively. This co-existence favors high TE performance because the light bands are useful to obtain good electrical conductivity while the heavy bands would provide a large effective mass as well as large Seebeck coefficient[47,48].

Intrinsically large Seebeck coefficient: The previous studies reported that GaTe has a large Seebeck coefficient of 873 μV K^{-1} for in-plane direction and 1233 μV K^{-1} for out-of-plane direction at 300 K. Because the Seebeck coefficient contributes square times in thermoelectric figure-of-merit, $zT = S^2\sigma T/\kappa$, the high S is an important plus point of GaTe as considered for thermoelectric applications.

Theoretically unexpecting good thermoelectric performance: Until now, existing reports on TE GaTe mostly are theoretical calculations. Bahuguna predicted a good zT of 0.85 at 300 K for GaTe monolayers[49], whereas Shangguan[36] reported a zT of 0.85 at 1100 K and 0.05 at 300 K for hexagonal and monoclinic structure, respectively. The newest published study by Li *et al.*[50] also proposed the high-performance TE potential for GaTe material with zT ~1.35 at 300 K. As a result, it is extremely desirable to investigate the TE properties of GaTe-based materials.

2.4.3. Current Challenges and Proposed Strategies

Despite having many properties with promising thermoelectric potential, it has several drawbacks restricting its thermoelectric performance.

Poor electrical conductivity: Pristine GaTe exhibits poor thermoelectric performance due to low carrier concentration around 10^{15} cm^{-3} at room temperature[51–54]. Our main aim is to manipulate the carrier concentration to achieve the ideal value, thereby increasing the TE efficiency of GaTe. As mentioned above, doping is a simple and effective strategy to enhance the TE properties via optimizing carrier concentration as well as decreasing the lattice thermal conductivity through enhancing phonon scattering[55,56]. Hence, the finding of suitable dopants for the GaTe system is the crucial key to not only for guiding the performance enhancement but also providing a deeper understanding of the material parameters.

Lack of a comprehensive study on thermal stability: From a practical point of view, a TE material should have excellent performance and good thermal stability at working temperatures. Basically, thermal stability is defined as the ability to against decomposition and/or transformation when prolonged exposure to high temperatures. Good thermal stability can ensure the durability and reliability for the responding devices at high temperatures for a long time. In general, the thermal stability of a given material is strongly influenced by intrinsic factors, such as structural phases and degree of crystallinity, which are associated with synthesis techniques, and extrinsic factors, such as gas atmosphere[57–61]. To date, most studies have focused on the stability of GaTe under ambient conditions. It was reported that GaTe demonstrates the poor environmental stability due to the oxygen intercalation between the layers[62]. Such behavior leads to the dramatic degradation in optical absorption and photoluminescence spectra after prolonged exposure to air. Numerous studies on the exposure time and oxidized layer thickness-dependency of GaTe have also been carried out in recent years[63,64]. Nonetheless, there is a lack of comprehensive studies on the thermal stability of GaTe at high temperatures under various gas atmospheres. Kotha[63] reported that no degradation or oxidation in GaTe flakes was found after annealing in pure oxygen environment at 200 °C. Whereas Fonseca[64] suggested that the rapid annealing in nitrogen at 300 °C helps to drive out oxygen molecules intercalated between vdW layers, therefore restoring the material properties as same as original states. So far, no further study on the thermal stability of GaTe at higher temperatures in different gases has been published. Thus, the need on studying the thermal stability of GaTe in different atmospheres is quite evident.

By using differential scanning calorimetry (DSC) and thermogravimetry analysis (TGA), we attempted to investigate the thermal decomposition and structural thermal stability of GaTe single crystals under nitrogen and argon atmospheres over a wide temperature range of 300 – 1173 K. The underlying mechanisms in thermally structure change were also explored. Furthermore, we clarified the influence of annealing temperature on structural and optical properties of GaTe material using Raman and photoluminescence spectroscopy.

Chapter 3. Experimental Section

3.1. Materials Fabrication

In this thesis, large-size high-quality single-crystalline gallium telluride (GaTe) were grown successfully using a temperature gradient technique, a member of "growth-from-the-melt" method group, including the Bridgman and Stockbarger techniques[65]. The Bridgman technique (**Figure 3.1a**) is characterized by the directional translation of the ampoule containing a melted mixture from the hot region to the cold region along the vertical furnace. In comparison, the Stockbarger technique is a more sophisticated modification of the Bridgman technique. In this technique, there is a high-temperature (upper) and a low-temperature (lower) zone separating by an adiabatic loss zone, as illustrated in **Figure 3.1b**. The melting point of the material is located within this lossy region, thereby achieving a larger axial gradient at the melt-solid interface than that of the Bridgman technique. These techniques have demonstrated numerous advantages, such as no seed requirement to initialize the crystal and the possibility of a high-quality single-crystal fabrication. However, there are several drawbacks that existed, such as the complexity, high-cost as well as difficulty in precisely controlling temperature by translating the ampoule and industrial scale-up. Therefore, developing a simple effective technique for growing high-quality single crystals in large size is demanded.

In principle, the temperature gradient technique (**Figure 1.6**) is similar to the Bridgman. In both techniques, the solidification rate (cooling rate) across the melting point is the most crucial factor for achieving single crystals. In contrast to Bridgman, there are no mechanical moving components in the temperature gradient technique, leading to easy setup and long-term working without maintenance. The formation of crystal initiates from the crystalline seeds at the bottom part when slowly lowering temperature across the melting point. The cooling rate is sophisticatedly controlled using a PID temperature controller with an accuracy of up to 0.1 K. This helps to maintain a constant solidification rate over the entire crystal, resulting in a homogeneous crystalline quality of single crystals.

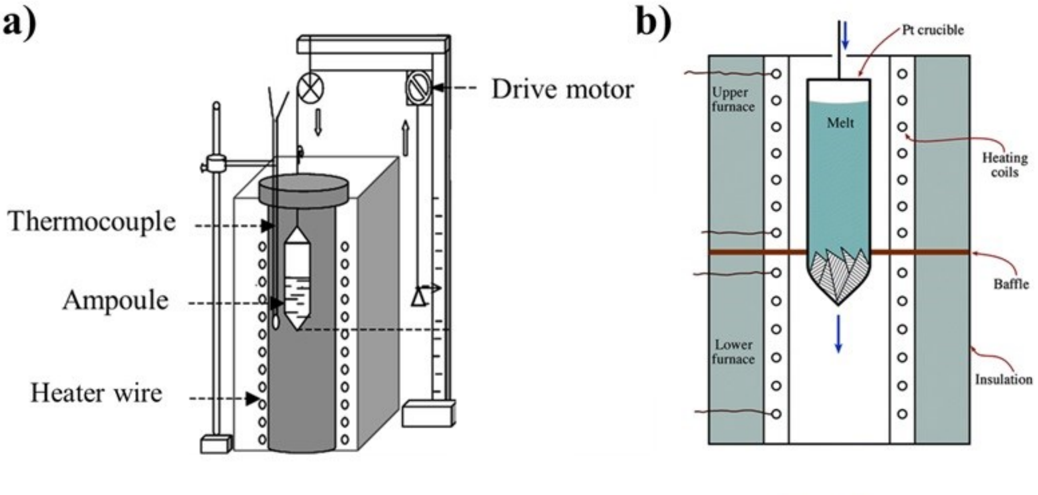

Bridgman

Stockbarger

Figure 3.1: Schematic of (a) Bridgman and (b) Stockbarger techniques.

High-purity (4N) raw elements (Ga, Te, and Bi) purchased from Alfa Aesar used as starting materials. Firstly, the raw constituent elements were weighed in a desired composition ratio, then mixed in quartz ampoules. The ampoules were evacuated under a pressure of 10^{-3} Torr, then sealed using a hydrogen-oxygen flame. Subsequently, these ampoules were placed in a modified vertical furnace, then gradually heated up to 1223 K, maintaining for 33 hours, followed by slowly cooling to 1023 K at a rate of 1 K h^{-1}. Finally, high-quality large-size GaTe single crystals were obtained after quickly cooling down to room temperature.

3.2. Material Characterization

3.2.1. X-ray Diffraction (XRD)

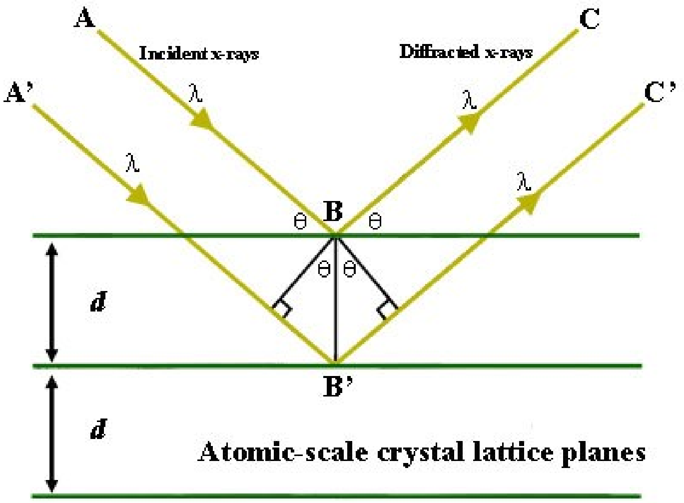

Figure 3.2: Schematic diagram illustrates the principle of X-ray diffraction.

X-ray diffraction (illustrated in **Figure 3.2**) is a powerful nondestructive technique for characterizing crystalline materials. It provides information on structures, phases, texture (preferred crystal orientations), average grain size, crystallinity, strain, and crystal defects. The diffraction of X-ray by crystals was discovered in 1912 by Max von Laue, then formulated by Lawrence Bragg in a simple mathematical form, known as Bragg law (**Equation 3-1**).

$$n\lambda = 2d \sin\theta \qquad (3-1)$$

Herein, λ denotes the wavelength of X-rays, d is the distance between two adjacent crystal planes (called planar spacing), θ is the angle between the incident ray and the sample surface (called Bragg angle), and n is an integer number, which describes the order of reflection. Well known that the wavelength of X-rays used in X-ray diffraction is in the vicinity of 1 Å, comparable to the range of interatomic spacing in crystals. Therefore, X-rays possess very high energy, suitable to detect the atomic arrangement within the crystal.

In this thesis, crystal structures of the obtained samples were characterized by using an X-ray diffractometer (Ultima IV, Rigaku Corporation, Japan) with a CuK$_\alpha$ radiation ($\lambda = 1.5418$ Å). The whole measurements were performed at room temperature in air.

3.2.2. Field Emission Scanning Electronic Microscopy (FE-SEM)

Field emission scanning electron microscope (FE-SEM) equipped with an energy dispersive spectroscopy (EDS) is also well known as a non-destructive technique used to investigate the morphology and element compositions within the materials in the submicron scale. FE-SEM uses a high-energy electron beam (0.1-30 keV) scanned across the sample surface, generating secondary electrons, backscattered electrons, and characteristic X-rays, as illustrated in **Figure 3.3**.

The imaging formed by detecting the secondary electron and backscattered electron signals present the topography of surface features, while the characteristic X-rays produce the information of element distribution. In this thesis, the layered structure, composition, and chemical homogeneity were characterized by field emission scanning electron microscope (JSM-7600, JEOL Ltd., Japan) at magnifications of 50,000×.

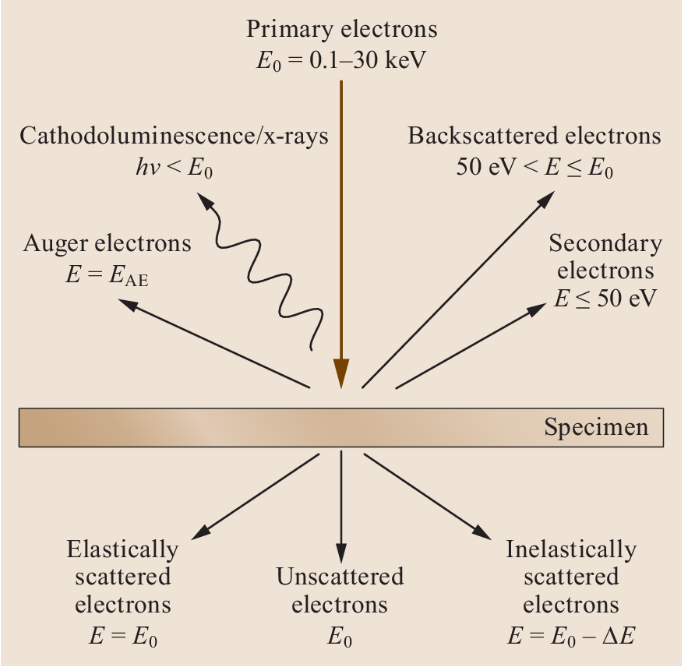

Figure 3.3: Schematic diagram illustrates the principle of field emission scanning electron microscopy.

3.2.3. Raman Spectroscopy

Raman spectroscopy is also a non-destructive chemical analysis technique used to determine the structures, phases, crystallinity, and molecular vibrational modes. Raman spectroscopy relies upon the inelastic scattering of photons induced by the interactions between the incident light and molecular vibrations in a material. The common light sources used in Raman scattering are usually from a laser in the visible (380-700 nm), near-infrared (800-2500 nm), or near-ultraviolet (10-400 nm) range. As interacting with molecules, most of the scattered light is at the same wavelength as the incident light - called Rayleigh scattering or elastic scattering (**Figure 3.4**). However, a small amount of light is scattered at different wavelengths, strongly depending on the chemical bonds – called Raman scattering or inelastic scattering. Therefore, the Raman peak associated with the wavelength shift would provide specific information about the chemical bond or molecular vibration. In this thesis, Raman spectroscopy were measured at room temperature using a micro-Raman microscope with a 532 nm excitation laser.

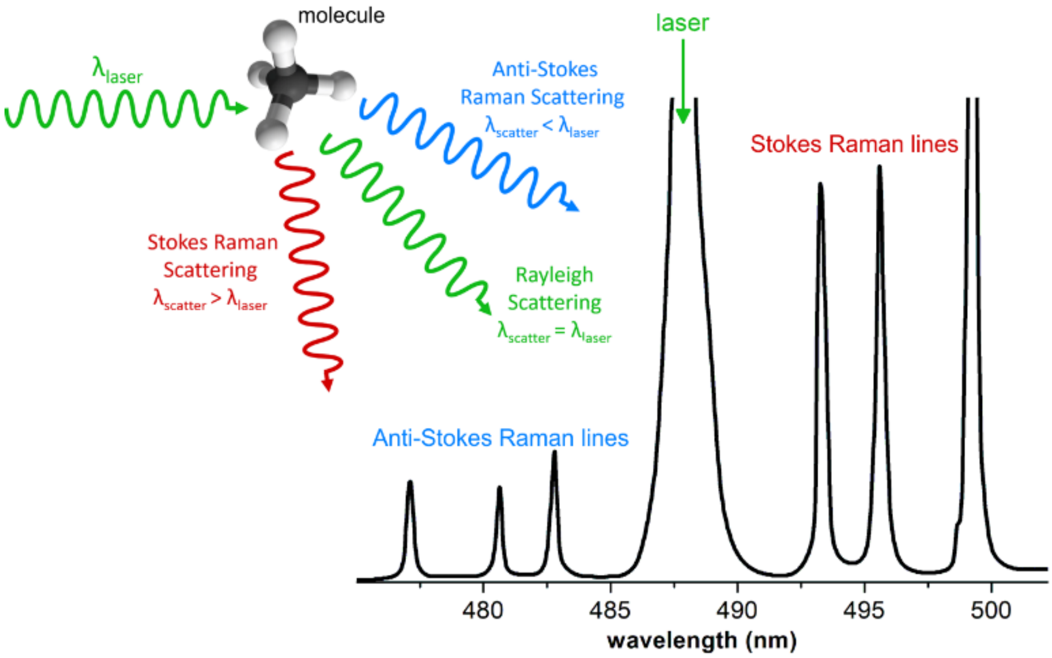

Figure 3.4: Schematic diagram illustrates the principle of Raman spectroscopy.

3.2.4. X-ray Photoelectron Spectroscopy (XPS)

X-ray photoelectron spectroscopy (XPS) is a surface-sensitive quantitative technique based on the photoelectric effect used to identify the presence of chemical elements as well as oxidation state, thereby revealing what other elements they are bonded to. In principle, the XPS spectrum is obtained by irradiating a material with a beam of X-rays (< 1.5 kV) in an ultrahigh vacuum environment of 10^{-9} Torr and measuring the kinetic energies of ejected electrons from the top layers of the material. The electron binding energy of each emitted electron can be determined by using the **Equation 3-2**:

$$E_{binding} = E_{photon} - E_{kinetic} \qquad (3-2)$$

where $E_{binding}$ is the smallest amount of energy required to remove an electron bound to nuclei in an atom - called the binding energy (BE), E_{photon} is the energy of the X-ray photons being used, and $E_{kinetic}$ is the kinetic energy of ejected electrons. It is well known that each core-level electron of an individual element is characterized by specific binding energy. Therefore, by measuring the binding energy, we can easily determine the constituent elements and oxidation states.

3.2.5. Photoluminescence Spectroscopy (PL)

Photoluminescence spectroscopy (PL) is a non-destructive technique to probe the electronic structure of materials. As illustrated in **Figure 3.5**, photoluminescence is a photo-excitation process that electrons absorb the incident lights, jumping to a higher electronic state, then release the photons when they return to a lower energy state. The PL peak energy is closely related to the energy level difference between the excited state and the equilibrium state. The peak intensity is quantified by the relative contribution of the radiative and nonradiative recombination. Therefore, PL spectroscopy is considered a powerful tool to qualify the defects and crystallinity of the material.

3.2.6. Ultraviolet – visible Spectroscopy (UV-Vis)

Ultraviolet-visible spectroscopy (UV-Vis) refers to the optical absorption process in that an electron can absorb a UV-Vis light, jump from the ground state to higher energy. The energy difference is exactly equal to the optical energy (called bandgap). In this thesis, the absorbance spectra were obtained by a UV-vis spectrophotometer (HP8453, Agilent, USA) at room temperature in air. The optical bandgaps were determined from the linear extrapolation of $(\alpha h\nu)^{\gamma}$ versus $h\nu$ plots with $\gamma = 2$ for the direct forbidden transition.

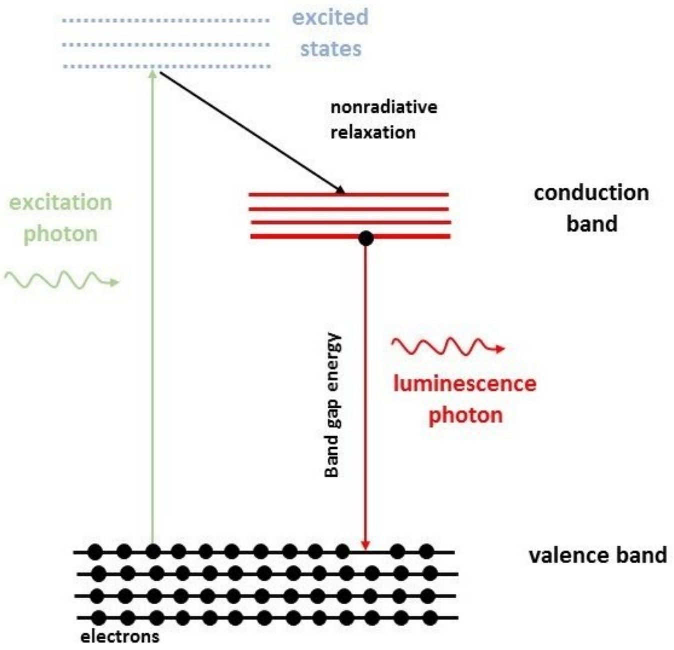

Figure 3.5: Schematic diagram illustrates the principle of photoluminescence spectroscopy.

3.2.7. Thermogravimetric Analysis (TGA) and Different Scanning Calorimetry (DSC)

Thermogravimetric analysis (TGA) is a thermal analysis that demonstrates the change in weight of a sample as a function of temperature. This measurement provides information about phase transitions, thermal decomposition, adsorption, oxidation, *etc.* It is also used to evaluate the thermal stability of the material in various environments, thereby proposing a suitable operating temperature range of its based devices.

Differential scanning calorimetry (DSC) is a technique measuring the difference of thermal energy per unit of time (heat flow) required to increase one Kelvin between a sample and reference material as a function of temperature. There are two different types of DSC: heat-flux DSC and power compensating DSC, as shown in **Figure 3.6**. In power compensated DSC, the sample and reference are placed in two thermally insulated furnaces. The temperature of the sample and reference is independently controlled to be equal throughout the experiment using two individual heaters. Then the difference in output power required to increase the temperature of the sample and reference is measured. In heat-flux DSC, the sample and reference are connected by a good thermal contact and placed together in a single furnace. The temperature difference is recorded as heating simultaneously the sample and reference in each time.

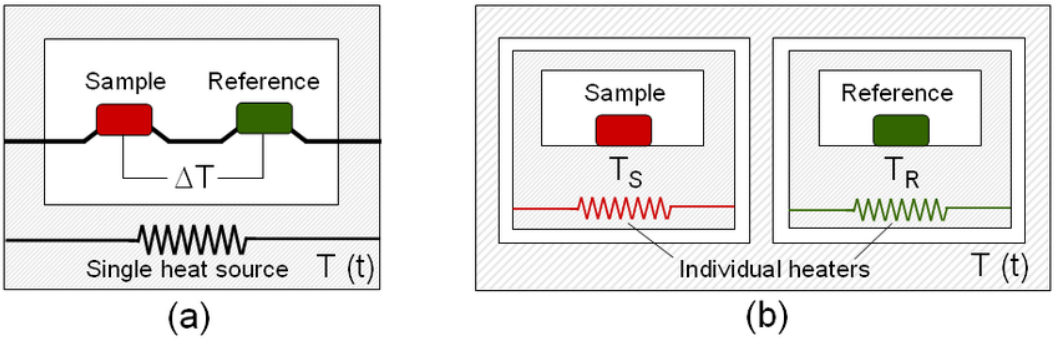

Figure 3.6: Schematic diagram illustrates the principle of (a) heat flux and (b) power compensated differential scanning calorimetry (DSC).

In this thesis, the thermal analysis measurements were performed under nitrogen (N_2) and argon (Ar) atmospheres in a wide temperature range of 300 – 1173 K using a differential scanning calorimeter (SDT Q600, TA Instruments, USA).

3.2.8. Electrical Conductivity and Seebeck Coefficient Measurements

There are a wide variety of techniques used to measure electrical conductivity, including two-probe and four-probe techniques (**Figure 3.7**). In the two-probe method, two electrodes are used for current input as well as for voltage measurement. The resistance (R) of the specimen between two electrodes can be determined using Ohm's law (**Equation 3-3**).

$$R = \frac{V}{I} \qquad (3-3)$$

where V and I are the voltage and current measured at two electrodes, respectively. The four-probe method is an alternative to the two-probe method in that the electrical current is passed through two outer electrodes while the voltage is measured from two inner ones. Comparing to the two-probe method, the four-probe method can eliminate the effects of contact resistance between the specimen and electrical contacts, therefore is more suitable and accurate. However, the contact resistance can still cause errors due to the Joule heating. Thus, it is imperative that the contacts should have low resistance.

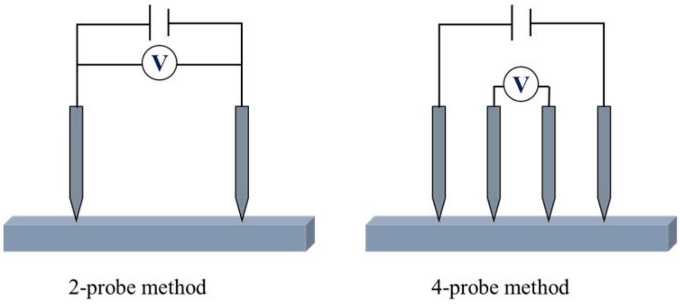

Figure 3.7: (a) Two-probe and (b) four-probe method for characterizing electrical conductivity of bulk samples.

In this method, four probes are usually collinear (in-line) and equidistant geometry. The electrical resistivity (ρ) and electrical conductivity (σ) are given by **Equation (3-4)** and **Equation (3-5)**, respectively:

$$\rho = R\frac{wt}{s} \qquad (3-4)$$

$$\sigma = \frac{1}{\rho} \qquad (3-5)$$

where s is the distance between two electrodes measuring the voltage, w is the width of specimen, and t is the thickness of specimen. To avoid the errors due to sample geometries and probe arrangement, a geometric factor has been proposed and described as a product of independent correction factors (**Equation 3-6**):

$$F = F_1F_2F_3 \qquad (3-6)$$

with F_1 correcting for the sample thickness, F_2 for the lateral dimensions, and F_3 for the relative placement of the probes on the sample. These correction factors have been derived and tested for a variety of probe arrangements and sample geometries. However, from the practical point of view, correction factors should generally be avoided whenever possible. Therefore, the sample is usually cut into a bar-shaped specimen with $l \geq 4s$ and $t \leq \frac{s}{2}$, where l is the length of specimen and s is the distance between two adjacent probes for ensuring the correction factors are approximately 1.

As mentioned in the section 1.2.1, Seebeck coefficient (S) describes the magnitude of the induced thermoelectric voltage (ΔV) in response to an applied temperature difference (ΔT) of a material. Clearly, the working principle of Seebeck coefficient measurement is quite simple and is nearly independent of the sample geometry. Conventionally, there are two common Seebeck measurement techniques, namely differential or integral methods. In the differential method, multiple ΔT and the corresponding ΔV values at a certain temperature are obtained. At that time, the Seebeck coefficient is extrapolated slope of the linear function of ΔV versus ΔT. In the integral method, one end of the specimen is held at a constant temperature (T) while the other is increased continuously up to $T + \Delta T$. The ΔV values are continuously measured, then the Seebeck coefficient is obtained from the slope of ΔV versus ΔT.

For Seebeck coefficient and electrical conductivity measurements, the obtained crystals were cut into the bar-shapes with dimensions of 2 × 2 × 9 mm^3 along the in-plane direction. Herein, we used the four-probe method for measuring electrical conductivity and the integral method for measuring the Seebeck coefficient at temperatures ranging from 300 to 700 K in a low vacuum environment of 10^{-3} Torr.

3.2.9. Thermal Diffusivity and Thermal Conductivity

Thermal diffusivity is a quantity characterizing the dispersive rate of heat throughout a given material. For measuring thermal diffusivity, the laser flash method (also known as laser pulse) is a common and effective method. The schematic measurement setup and procedure is shown in **Figure 3.8**. In this LFA technique, the front surface of a sample is heated by a laser pulse. As a result, the temperature of the sample's rear face rises due to the thermal diffusivity. The resulting temperature rise is recorded as a function of time using the infrared (IR) radiation and IR detector. Assuming that the heat is diffused along one direction, the thermal diffusivity can be determined from this temperature rise using **Equation (3-7)**:

$$D = 0.1388 \frac{L}{\frac{t}{2}} \qquad (3-7)$$

where D is the thermal diffusivity of material, L is the sample thickness, and t is the time, at which the maximum temperature reached.

By knowing the mass density (ρ) and the specific heat capacity (C_p) of the sample, the thermal conductivity can be calculated with the following **Equation (3-8)**.

$$\kappa = D\rho C_p \qquad (3-8)$$

The LFA method is a rapid and non-destructive measurement that able to measure low-to-high thermal conductivity materials. Furthermore, the required specimen geometry is simple and small samples with an easy preparation can be investigated. In this thesis, the samples were cut into disk-shaped specimens with dimensions of 14 × 14 × 2 mm^3 for thermal diffusivity measurement at temperatures ranging from 300 to 700 K in the argon atmosphere using commercial equipment (LFA-457, NETZSCH, Germany).

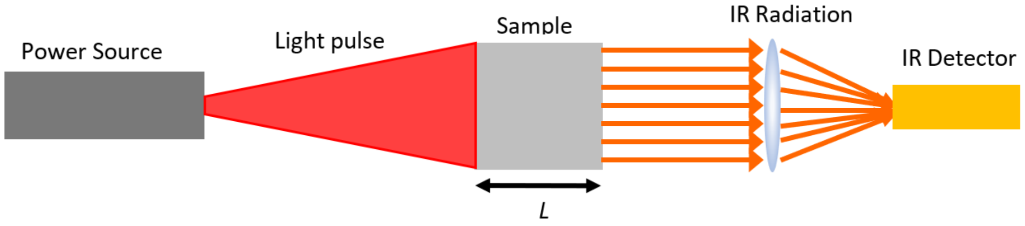

Figure 3.8: Laser flash analysis (LFA) method scheme.

3.2.10. Hall Effect Measurement

Edwin Hall, a physicist, was the inspiration for the Hall-effect theory in 1879. He discovered that as passing an electric current through a conductor in a magnetic field, the magnetic field exerts a transverse force on the traveling charge carriers, pushing them to one side of the conductor (**Figure 3.9**). This causes a potential difference between the two sides due to a difference in charge carrier concentration. This difference in potential is known as the Hall voltage (V_H), and this phenomenon is called the Hall effect. The Hall voltage is given by **Equation (3-9)**

$$V_H = \frac{I_x B_z}{n_H t e} \qquad (3-9)$$

where n_H is the carrier concentration, t is the sample thickness, e is the electron charge, I_x is the electric current, and B_z is the external magnetic field. Thus, the carrier concentration can be determined by measuring the Hall voltage induced by the applied magnetic field.

The van der Pauw method is a widely used technique for determining the Hall coefficient ($R_H = \frac{V_H}{I_x}$) as well as carrier concentration of a sample. The van der Pauw able to accurately measure the properties of a sample with any arbitrary shape, as shown in **Figure 3.10**, if its thickness is much smaller than its width and length.

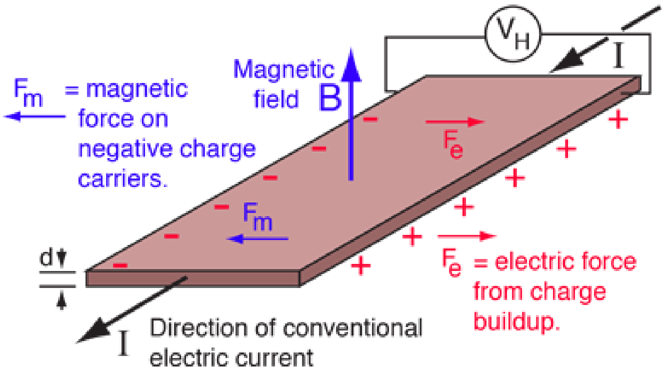

Figure 3.9: Schematic diagram illustrating the principle of Hall effect.

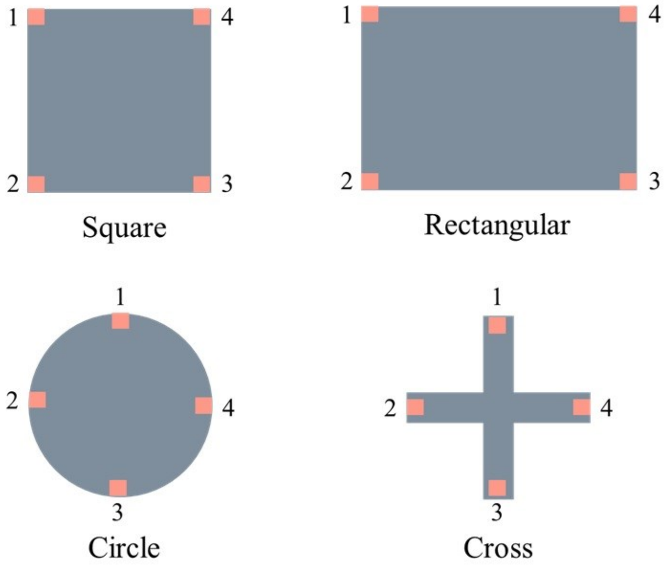

Figure 3.10: Common van der Pauw sample geometries: (a) square, (b) rectangular, (c) circle, and (d) cross shape.

However, the van der Pauw method prefers to employ a four-point probe in the square shape. In principle, isotropic, homogeneous, smooth, uniform thickness, and free of island hole defects are all requirements. As described in **Figure 3.11**, the contacts are numbered from 1 to 4 in counterclockwise order beginning at the top-left contact. With a positive magnetic field, the current I_{13} is applied to the sample and the voltage V_{42} is measured, then this is repeated for I_{24} and V_{13}. In practice, offsets in the instruments and contact resistance can cause a variety of errors. These errors do not depend on the current and can be corrected by using the current reversal. Similarly, a magnetic field reversal is often used to cancel the offsets from measuring the external magnetic field. For each given magnetic field value, the average coefficient is determined by **Equation (3-10)**.

$$R_H = \frac{\mathrm{V}_{42} + \mathrm{V}_{24} + \mathrm{V}_{13} + \mathrm{V}_{31}}{4I} \qquad (3-10)$$

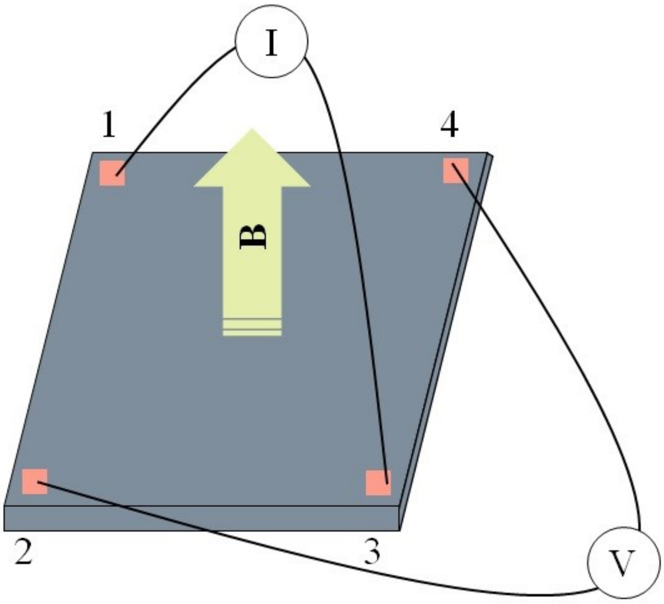

Figure 3.11: Van der Pauw sample with square contacts.

The carrier concentration of a material is linearly extrapolated from the slope of R_H versus B_z plot using **Equation (3-11)**:

$$n_H = \frac{1}{Ate} \qquad (3-11)$$

where A is the slope of R_H versus B_z plot. At that time, the carrier mobility (μ_H) can be determined by **Equation (3-12)**.

$$\sigma = n_H \mu_H e \qquad (3-12)$$

In this thesis, the resulting samples were cut into a square shape with dimensions of ~5 × 5 × 0.5 mm^3 for Hall effect measurement through van der Pauw (vdP) configuration under a reversible magnetic field of 0.45 Tesla using a home-build measurement system.

Chapter 4. Thermal Stability on Crystal Structure of Single-crystalline GaTe under Various Inert Atmospheres

4.1. Introduction

The thermal stability of GaTe single crystals under different inert atmospheres, such as nitrogen (N_2) and argon (Ar), is discussed in this chapter. High-quality GaTe single crystals were successfully synthesized using the temperature gradient technique, as described in detail above. The monoclinic structure with space group $C2/m$ (No. 12) was confirmed by XRD measurement for both powders and cleaved planes. SEM equipped with EDS technique were used to characterize the surface morphology and chemical composition of samples. In addition, the bandgap and crystallinity of GaTe cleaved specimens were evaluated using room-temperature optical absorbance and PL spectra. A comprehensive study on thermal stability of GaTe crystal structure was carried out using the DSC and TGA analysis under N_2 and Ar atmospheres over a wide temperature range of 300 – 1173 K. Our findings suggested that single-crystalline GaTe is thermally stable up to 700 K in Ar and 935 K in N_2. This difference was explained by the physical adsorption of N_2 molecules on GaTe surface, consequently protecting the material from thermal decomposition[66]. Furthermore, the effect of thermal treatment on crystallinity was investigated using PL and Raman spectroscopies on GaTe samples annealed under N_2 gas at 573, 673, 773, and 873 K. Three prominent Raman modes at 97, 145, and 158 cm^{-1} according to the monoclinic phase nearly unchanged, indicating no structural transformation. The PL intensity increases as rising annealing temperature, reaching a peak at 673 K, due to the crystallinity improvement. We detected a substantial decrease in PL intensity at 873 K, which is attributed to vacancies caused by tellurium evaporation.

4.2. Results and Discussion

4.2.1. Morphological and Structural Analysis

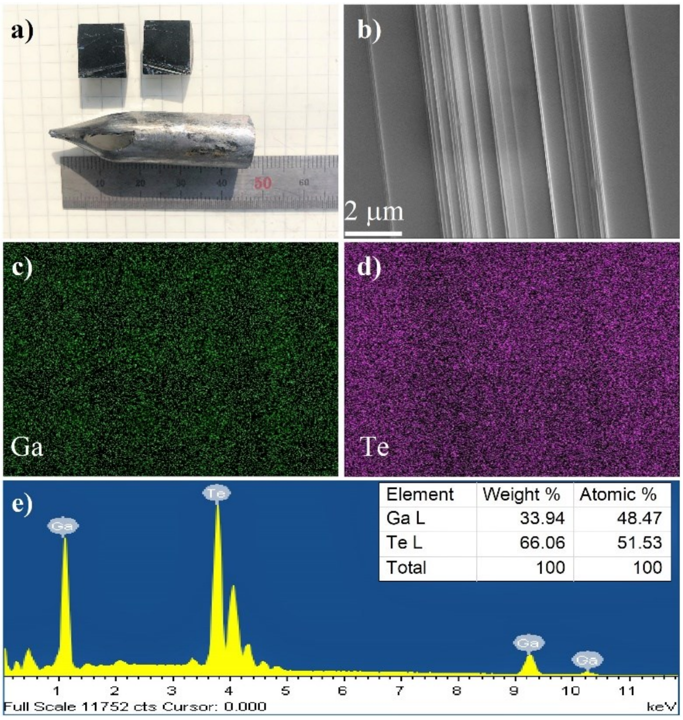

Element	Weight %	Atomic %
Ga L	33.94	48.47
Te L	66.06	51.53
Total	100	100

Figure 4.1: (a) Photograph of the as-grown GaTe single crystal, (b) SEM image (surface view), EDS mapping for (c) Ga and (d) Te, and (e) EDS spectrum. Scale bar is 2 μm.

Figure 4.1a shows a representative of single-crystalline GaTe sample, grown by using the temperature gradient technique, with a flat and shiny surface. As shown in **Figure 4.1b**, the SEM image demonstrates a stair structure consisting of micro-lamellas, a consequence of exfoliation using scotch tape during the sample preparation for measurement. This observation indicates the naturally layered structure of GaTe crystals. The EDS spectrum (**Figure 4.1e**) confirmed the stoichiometry of GaTe compounds with Ga: Te ratio of 1.00: 1.06. The EDS mapping showed the homogeneous contribution of constituent elements without any segregation, as shown in **Figure 4.1c** and **Figure 4.1d**.

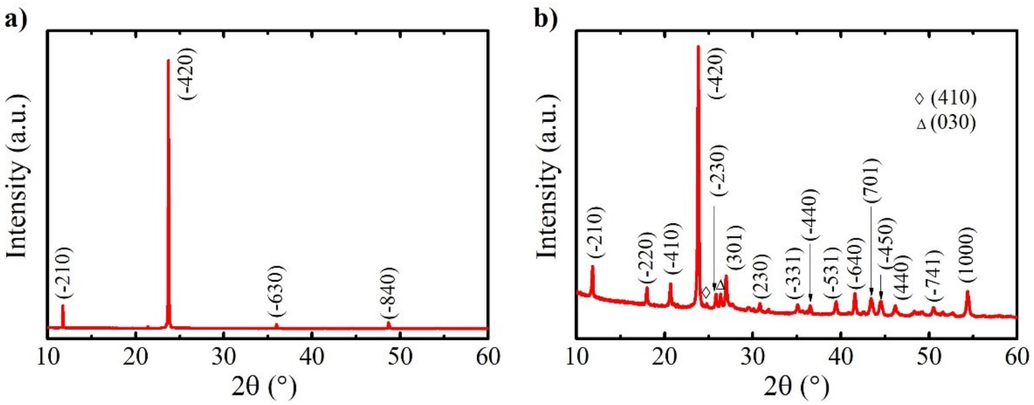

Figure 4.2: XRD patterns for (a) cleaved planes and (b) powders.

The XRD patterns on the cleaved plane and powder of GaTe are presented in **Figure 4.2**. All diffraction peaks are sharp and well-identified to the monoclinic GaTe structure with space group $C2/m$ (JCPDF No. 71-0620). No secondary impurity phases were found within the detection limit, confirming the high purity of our GaTe samples. Clearly, all peaks in **Figure 4.2a** are highly oriented to the $[\bar{2}10]$ direction, indicating high crystallinity. From the powder XRD pattern (**Figure 4.2b**), the lattice parameters were calculated to be $a = 17.281$ Å, $b = 10.423$ Å, $c = 4.063$ Å, and $\gamma = 104.011°$, which are highly consistent with the earlier report[67].

4.2.2. Optical Characterization

To clarify the energy gap, the room-temperature absorbance and PL spectra of GaTe were performed in ambient condition. **Figure 4.3a** shows a strong peak around 742 nm in the UV-vis spectrum (solid line), indicating absorption of the red-light region. The dependence of the absorption coefficient as a function of energy for a direct gap is given by Tauc's relation (**Equation 4-1**):

$$(\alpha h\nu)^2 = A\left(h\nu - E_g\right) \qquad (4-1)$$

where A is a constant, h is the Planck constant, ν is the light frequency, α is the absorption coefficient, and E_g is the energy gap. The energy gap is linearly extrapolated from the plot of $(\alpha h\nu)^2$ versus $h\nu$ to be 1.646 eV, which is in accordance with reported values[68–71]. The recorded PL spectrum (open circle) only shows a broad asymmetric peak at 1.619 eV. Furthermore, no other peaks were found within the instrument's detection limit.

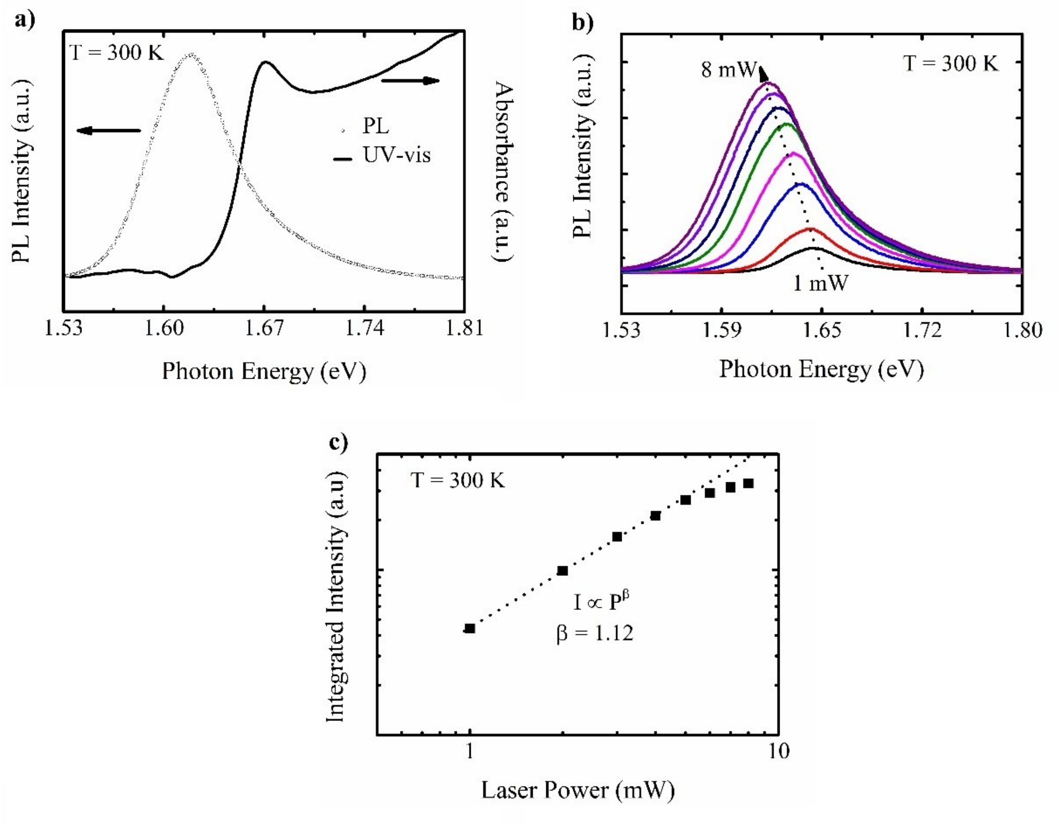

Figure 4.3: (a) Room-temperature absorption (solid line) and PL (open circle) spectra. (b) Power-dependent PL spectra at room temperature. (c) The log-log plot of the integrated PL intensity versus laser power.

To explore the recombination mechanism of excitons, we conducted the power-dependent PL of GaTe cleaved surfaces. As shown in **Figure 4.3b**, the photon energy shifts toward lower energies (red shift) with increasing the laser power, while the FWHM slightly increases (not presented in this thesis). In direct-bandgap semiconductors, the PL intensity (I_{PL}) is related to the laser power (P) following the **Equation (4-2)**:

$$I_{PL} \propto P^{\beta} \tag{4-2}$$

with the exponent factor $\beta = 2$ for band-to-band excitons, $1 < \beta < 2$ for free- or bound-excitons, and $\beta < 1$ for defect-related excitons (free-to-bound or donor-to-acceptor transition)[72]. **Figure 4.3c** describes the plot of integrated PL intensity versus laser power for GaTe cleaved planes at room temperature with $\beta = 1.12$., suggesting that the observed emission band is induced by the recombination of near-band-edge excitons. Based on XRD, SEM, and PL results, it is clearly affirmed that layered single-crystalline GaTe grown by the temperature gradient technique exhibit excellent crystallinity.

4.2.3. Structural Thermal Stability in Various Atmospheres

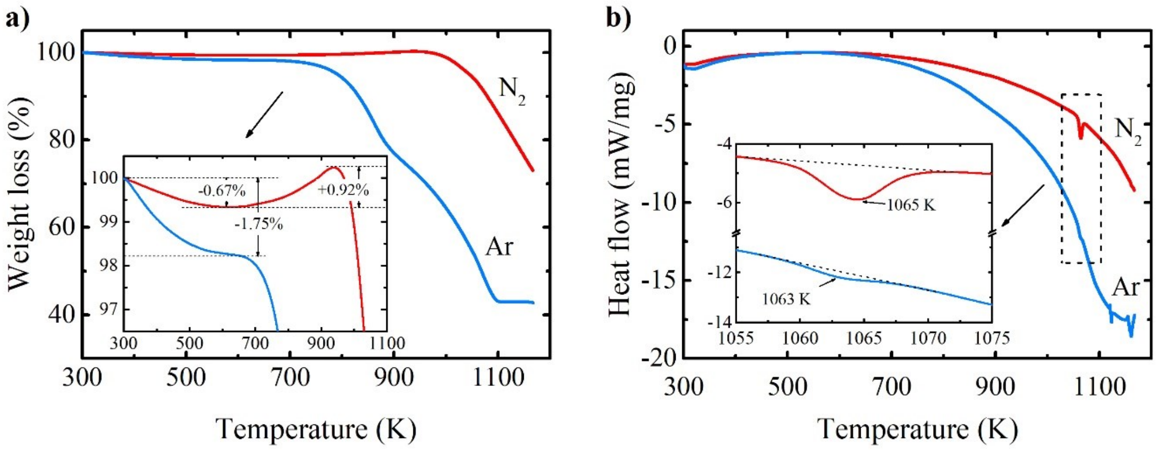

Figure 4.4: (a) TGA and (b) DSC thermograms of GaTe single crystals in N_2 (red line) and Ar (blue line).

TGA and DSC analysis were conducted in the temperature range of 300-1173 K under N_2 and Ar atmospheres to investigate the thermal properties of GaTe single crystals in different environments. In the N_2 atmosphere (**Figure 4.4a**), the weight of GaTe decreases by 0.67% as rising temperature up to 623 K, then increases by 0.92% as increasing temperature up to 935

K, and finally decreases sharply with temperature. Clearly, the TGA curve in the Ar also shows a small weight loss of 1.75% in the temperature range of 300 – 700 K, then undergoes a two-step decomposition until 1100 K. The initial weight loss in TGA curves for both N_2 and Ar gases is caused by the evaporation of water molecules and other volatiles on the sample surface. Surprisingly, we found a weight gain when performing thermal analysis in the N_2 atmosphere, while no such observations were observed in Ar. N_2 is well known as a diatomic gas, forming by a triple covalent bond between two nitrogen atoms (N-N), thus, possesses a quadrupole moment because of the unequal charge distribution within the molecule. Whereas argon is monatomic, therefore, no such electric moment existed in Ar atoms. Furthermore, we assumed that surface Te atoms are polarized due to inhomogeneous charge distribution. Thus, N_2 molecules might easily attached to tellurium atoms via the weak electrostatic forces. As a result, N_2 physically adsorbed layers not only acted as shielding layers, preventing thermal decomposition, but also resulted in a weight gain at temperatures ranging from 623 to 935 K. This effect is unexpected to happen in the case of argon gas due to the lack of a quadrupole moment in Ar monatomic.

When the temperature exceeds 700 and 935 K for the Ar and N_2 cases, respectively, the sample weight rapidly decreases caused by tellurium volatilization. The sample only undergoes a one-step thermal decomposition in N_2, while a two-step degradation was observed in Ar atmosphere. Using the derivative weight thermometric curve (DTG), the temperature at which the maximal decomposition rate occurs is determined to be 862 and 1070 K for argon and 1062 K for nitrogen (**Appendix A.1**).

Figure 4.4b shows the temperature dependence of heat flow spectra in both N_2 and Ar atmospheres. Clearly, DSC thermograms present a sharp endothermic peak near 1065 and 1063 K, respectively, according to the dramatic weight losses as shown in the TGA curves. These peaks are corresponding to the melting point of GaTe. Otherwise, no phase transitions or chemical formations are observed in DSC curves, suggesting a high thermal stability of GaTe.

4.2.4. Influence of Thermal Treatment on Crystal Structure

Herein, we performed the room-temperature Raman and PL measurements for all samples, which were annealed at different temperatures (T_a): 573, 673, 773, 873 K in N_2 gas for 60 minutes, to gain insight into the impact of heat treatment on structural properties. The surface morphology of annealed samples was examined using an optical microscope with a magnification of x100, as seen in **Figure 4.5a**. For T_a < 873 K, the microscopic images show uniform and crack-free surfaces. For T_a > 873 K, the surface is inhomogeneous with the presentation of yellow-dark areas (A) and clean regions (B).

The as-prepared GaTe sample demonstrates Raman peaks at 91, 97, 109, 145, and 158 cm^{-1}, as seen in **Figure 4.5b**. Almost peaks are well assigned to the active modes of monoclinic phase as reported by Liu[68], Zhao[73], and Yamamoto[74], except for an abnormal peak at 91 cm^{-1}. Among them, the peak at 158 cm^{-1} is associated with the B_g mode, while the rest is attributed to A_g mode. For the abnormal Raman peak at 91 cm^{-1}, unfortunately, we failed to identify the vibrational origin. However, this peak obviously does not match any active modes corresponding to the oxidation phases, such as TeO_2[75], Ga_2O_3[76], and/or hexagonal GaTe structure[73]. When T_a < 873 K, three predominant peaks nearly unchanged with increasing annealing temperature. This indicates an excellent thermal stability on crystal structure of GaTe material. When the annealing temperature reached 873 K, only two peaks at 106 and 123 cm^{-1} were seen in the Raman spectrum, which is measured in region A. The peak at 106 cm^{-1} clearly corresponds to the Raman mode of bulk monoclinic GaTe. The extra peak at 123 cm^{-1} is seemly associated to the TeO_2 phase formation[75] after annealing at 873 K. This peak might result from the unavoidable residual oxygen amount in the annealing system. On the other hand, no other peaks related to other transformations was observed. In the clean region B, the Raman spectrum is similar with those of samples annealed at lower temperatures.

Figure 4.5c presents the room-temperature PL spectra for all as-prepared and annealed samples with a strong PL emission observed around 1.623 – 1.636 eV. It can be seen clearly that the PL intensity increases with annealing temperature, reaching a maximum value at T_a = 673 K, then decreases sharply at higher annealing temperatures (**Figure 4.5d**). The increase in PL intensity with annealing temperature is attributed to a crystallinity enhancement in GaTe material. Tellurium is a well-known volatile element with a higher saturated vapor pressure than that of gallium[77]. In particular, the vapor pressure is ~10^{-1} and ~10^{-11} Torr at 700 K, then increasing up to ~10^{1} and 10^{-7} Torr at 900 K for tellurium and gallium, respectively. Therefore, the formation of tellurium vacancies is rather favorable than that of gallium vacancies when T_a < 900 K. Based on the preceding claims, the decrease in PL intensity at 773 and 873 K can be due to tellurium vacancies caused by high-temperature tellurium volatilization. Furthermore, for the sample annealed at 873 K, we observed the absence of PL emission in region A. This annihilation is caused by GaTe surface oxidation, which corresponds to the Raman peak 123 cm^{-1} induced by TeO_2 formation.

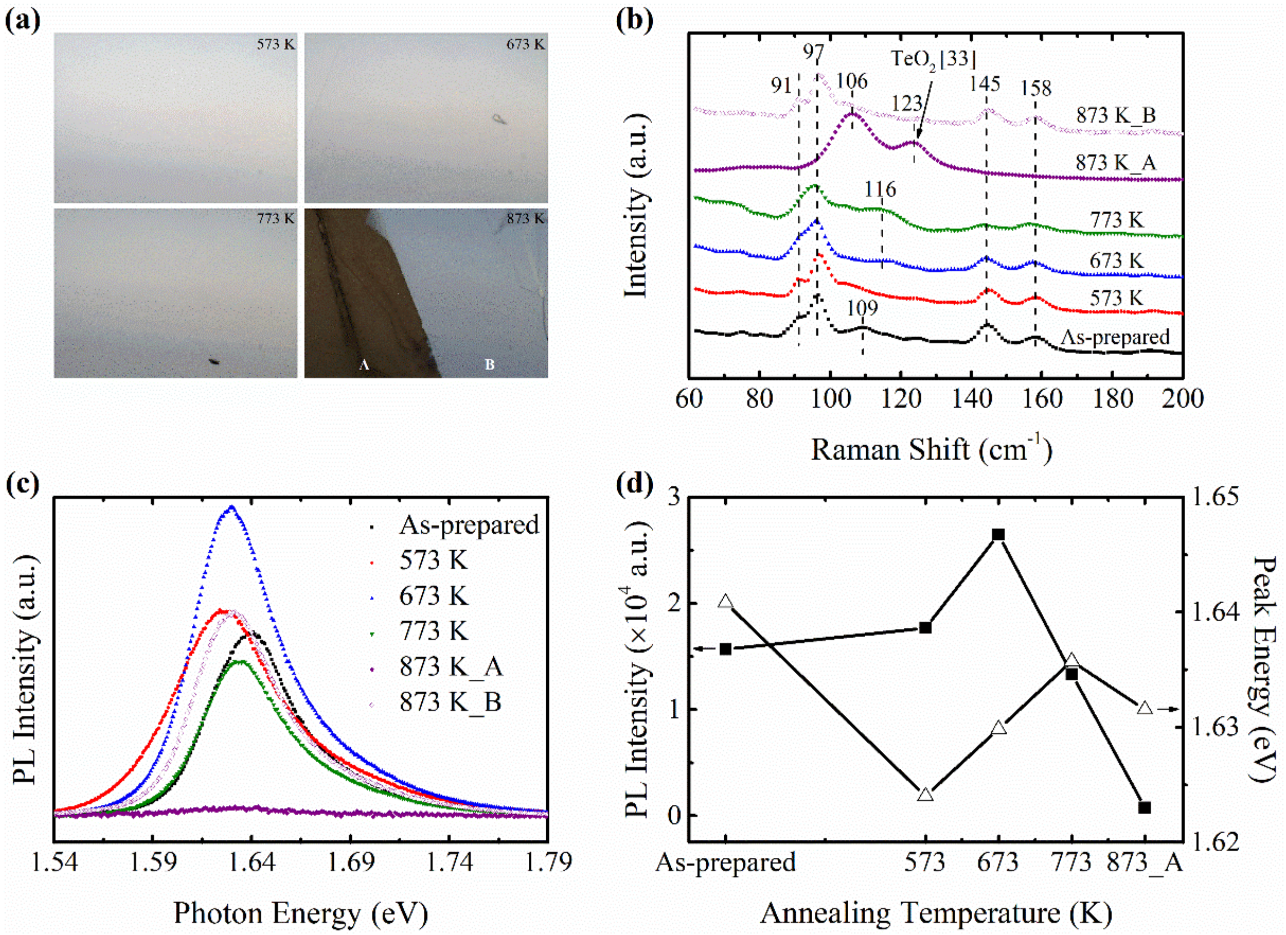

Figure 4.5: (a) Optical microscopic images. Room-temperature (b) Raman and (c) PL spectra of the as-prepared and annealed GaTe samples. (d) The dependence of PL intensity and peak energy as a function of annealing temperature.

4.3. Conclusion

To summarize, the temperature gradient technique was used to successfully develop GaTe single crystals with high crystalline efficiency. The obtained samples showed a monoclinic layered structure of GaTe with the lattice parameters calculated to be $a = 17.281$ Å, $b = 10.423$ Å, $c = 4.063$ Å, and $\gamma = 104.011°$. The power-dependent PL spectra revealed that near-band-edge exciton recombination play a dominant contribution in GaTe crystals. We found that GaTe is thermally stable up to 935 K in N_2 and 700 K in Ar without any structural phase transformation. The greater thermal stability of GaTe in the nitrogen atmosphere was a consequence of the N_2 physical adsorption, preventing GaTe material from surface damage. We also investigated the improvements in structural and optical properties of GaTe materials by thermal treatment. No structural damage occurred during annealing at temperatures lower than 873 K. Furthermore, the thermal treatment promoted a significant increase in PL intensity, originated from the improved crystalline quality. This research would provide an efficient synthesis technique for obtaining high-quality crystalline GaTe crystals, as well as thermal stability information for researchers interested in using GaTe for solar cells and thermoelectric applications.

Chapter 5. Enhancing Thermoelectric Properties of GaTe Single Crystals via Bi Doping

5.1. Introduction

In this chapter, we attempt to synthesize and enhance the TE properties of single-crystalline GaTe via doping. Herein, bismuth (Bi) was chosen to replace Te sites for increasing carrier concentration, consequently enhancing TE performance of GaTe material. We have successfully synthesized Bi-doped samples using the temperature gradient method. Acting as acceptors, Bi atoms helped in increasing hole concentration from 9.43×10^{15} cm^{-3} for the pristine GaTe to 1.63×10^{17} cm^{-3} in BGT-4 samples. Bi also acts as a chemical agent, which helps to enhance crystallinity. Thus, carrier mobility increased with increasing doping concentration, reaching 68.25 cm^{2} V^{-1} s^{-1} in the BGT-4 sample. As a result, the electrical conductivity and power factor (PF) of BGT-4 crystals achieved maximum values of 3.62 S cm^{-1} and 1.21 W cm^{-1} K^{-2} at 500 K, respectively. Consequently, the maximum electrical conductivity and power factor (PF) were obtained as high as 3.62 S cm^{-1} and 1.21 W cm^{-1} K^{-2}, respectively, for BGT-4 samples at 500 K. Meanwhile, Bi doping has negligible influence on the thermal properties of single-crystalline GaTe samples. Collectively, a maximum zT value of ~0.02 was reached at 700 K for the BGT-4 sample[78].

5.2. Results and Discussion

5.2.1. Investigation of Carrier Concentration and Mobility

Table 2 presents the carrier concentration (p) and mobility (μ) of all samples, which were calculated from the Hall effect measurements at room temperature. As shown in **Appendix**

A.2, all samples demonstrates a positive slope of the Hall coefficient (R_H) versus magnetic field (B), indicating the p-type conduction. The hole concentration of the pristine sample is 9.43 × 10^{15} cm^{-3}, which is considerable to the previous reports[51,53]. The presentation of Bi atoms in the GaTe matrix promotes to increase the hole concentration, indicating that bismuth atoms behave as acceptors. The hole concentration increases with Bi doping concentration, as predicted, and is 0.63, 0.90, 1.20, and 1.63 × 10^{17} cm^{-3} for BGT-1, BGT-2, BGT-3, and BGT-4 samples, respectively. These values were used to differentiate samples in this work.

Table 2: Hole mobility (μ), hole concentration (p), and thermal activation energy (E_a) of the pristine and Bi-doped GaTe single crystals.

Samples	Raw molar ratio Ga: Te: Bi	Carrier concentration p (cm^{-3})	Mobility μ (cm^2 V^{-1} s^{-1})	E_a (meV)
Pristine GaTe	1.00: 1.00: 0.00	9.43 × 10^{15}	27.78	82
BGT-1	1.00: 1.00: 0.005	6.30 × 10^{16}	27.84	74
BGT-2	1.00: 1.00: 0.02	9.00 × 10^{16}	38.19	68
BGT-3	1.00: 1.00: 0.05	1.20 × 10^{17}	56.77	66
BGT-4	1.00: 1.00: 0.08	1.63 × 10^{17}	68.25	60

To investigate chemical homogeneity, the room-temperature hole concentration for the BGT-4 sample as a function of sample length was measured (**Appendix A.3**). Clearly, the sample has a similar carrier concentration over the entire sample with an average value of ~1.64 ± 0.04 × 10^{17} cm^{-3}, indicating a homogeneous composition. Furthermore, the hole concentration of samples with greater initial Bi addition is comparable to that of BGT-4 to sample (not shown). This shows the upper Bi doping limit in GaTe material. Surprisingly, because of impurity scattering effect, mobility usually decreases with rising carrier concentration. However, Bi doping improves not only the hole concentration but also the hole mobility from 27.84 to 68.25 cm^2 V^{-1} s^{-1} for the pristine GaTe and BGT-4 samples, respectively. This increase in hole mobility can be explained by the crystallinity improvement, which will be discussed further below.

5.2.2. Crystal Structure and Morphology

Figure 5.1a depicts a real photo representative for single-crystalline Bi-doped GaTe with cleaved shiny surfaces. Main diffraction peaks in the XRD patterns of cleavage planes (**Figure 5.1b**) well oriented along $(\bar{2}10)$ direction, indicating a highly oriented layered crystal structure. The layered structure was also confirmed through FE-SEM image (seen the inset of **Figure 5.1b**), which demonstrates a surface morphology consisting of micro stair-like lamellas. To characterize Bi doping effects on the structural properties, powder XRD patterns were performed for all samples. As displayed in **Figure 5.1c**, all peaks are indicated to the monoclinic structure with space group $C2/m$ (JCPDS #71-0620). No secondary phases are detected, suggesting the high purity of samples.

As shown clearly in the enlarged XRD patterns (**Figure 5.1d**), the diffraction peak in the vicinity of 23.8° slightly shifts to lower 2θ with the addition of Bi. The lattice constants for the pristine GaTe were determined to be $a = 17.401$ Å, $b = 10.481$ Å, and $c = 4.079$ Å, increasing upon the rising Bi content (**Table 2**), which corresponds to the peak shift. Assuming Bi atoms intercalated between vdW layers, the lattice constants a and b should be almost remained, and the lattice constant c should be significantly expanded. If contrasting, Bi substitutes the host atoms, the lattice constants would be simultaneously increased because the larger atomic radius of Bi (1.60 Å) compared with Ga (1.30 Å) and Te (1.40 Å). Thus, the substitution of host atoms by Bi causes to the unit-cell expansion of GaTe lattice.

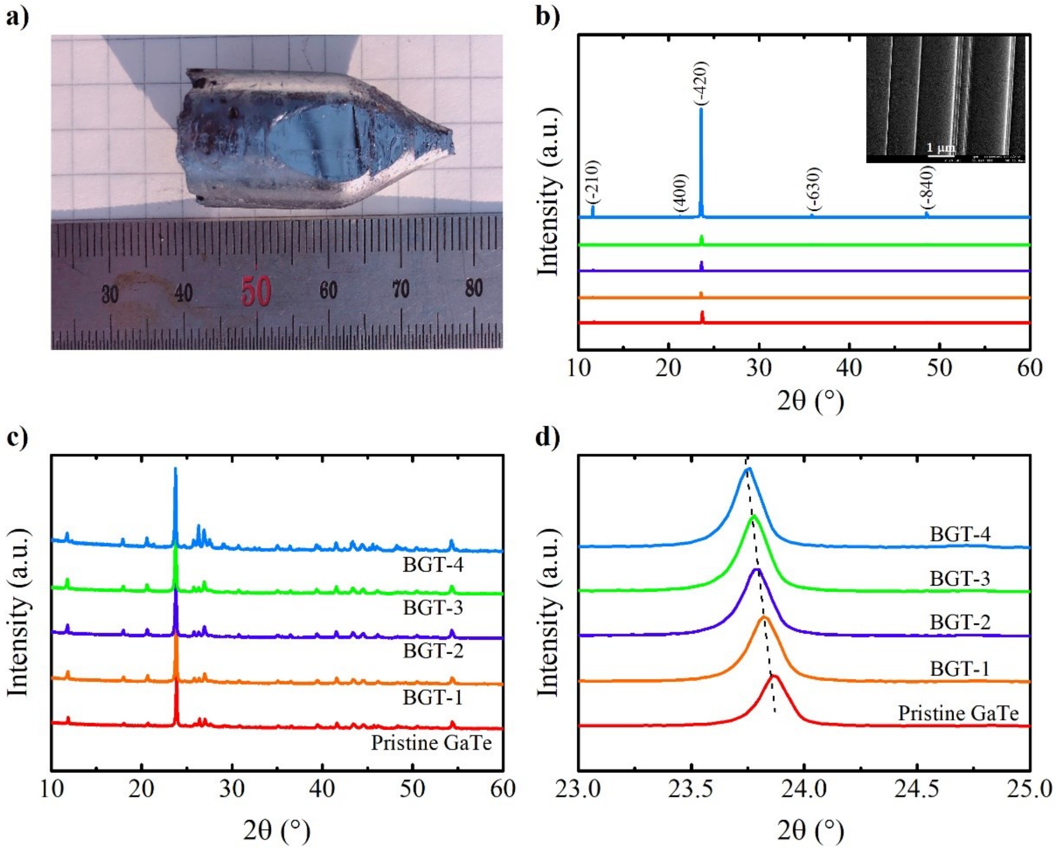

Figure 5.1: (a) Representative photograph of a GaTe crystal. XRD patterns for (b) cleaved surfaces and (c) powders of the pristine GaTe and Bi-doped single crystals. Inset reveals the surface SEM image. (d) Enlarged view of XRD patterns reveal a lower 2θ shift of $(\bar{4}20)$ peaks.

Table 3: Structure constants of the pristine GaTe and Bi-doped samples.

Samples	a (Å)	b (Å)	c (Å)	FWHM (°)
Pristine GaTe	17.401	10.481	4.079	0.168
BGT-1	17.428	10.488	4.089	0.160
BGT-2	17.445	10.505	4.095	0.156
BGT-3	17.448	10.516	4.096	0.154
BGT-4	17.465	10.534	4.103	0.124

Furthermore, as the Bi doping concentration increased, an undeniable decrease in FWHM was observed, which agrees well with the PL intensity enhancement (**Appendix A.5**). These findings can be understood by the significant crystallinity enhancement. To achieve the thermodynamic equilibrium, natural defects were generally created inside crystal during the solidification procedure. These native defects will cause lattice distortions, affecting crystallinity, and act as scattering centers, limiting the carrier mobility. In GaTe material, Bi not only acts as acceptor but also act as a chemical agent, called flux, that helps to reduce the melting point of GaTe material as well as remove oxidized surface. Thus, the natural defects could be eliminated with the introduction of Bi, enhancing the crystallinity and carrier mobility.

5.2.3. Doping Mechanism

To gain further insights into the doping mechanism, we investigated the vibrational modes of pristine GaTe and BGT-4 crystals using Raman spectroscopy. The shifting of Raman peaks is caused by the atomic mass and/or radius difference between host atoms and dopants. In detail, if an atom is occupied by a larger-mass atom, resulting Raman peaks shift to a lower vibrational frequency, following **Equation (5-1)**:

$$\nu = \frac{1}{2\pi}\sqrt{\frac{k}{M}} \qquad (5-1)$$

where k is the stiff ness, ν is the vibrational frequency, and M is the atomic mass. All Raman spectra show five peaks at 114.9, 163.9, 176.5, 208.5, and 268.8 cm^{-1} (**Figure 5.2**,), which agree well with the early reports[41,66,79]. Interestingly, the Raman peak at 114.9 cm^{-1} shifts ~2 cm^{-1} to lower wavenumbers (redshift) in the BGT-4 sample (**Figure 5.2b**). In addition, no significant change was observed in others. **Figure 5.2c** depicts a schematic illustration of vibrational modes in GaTe. Clearly, the vibration of gallium atoms is responsible for the two active modes at 208.5 and 268.8 cm^{-1}, while the vibration of tellurium atoms mainly contributes to the peak at 114.9 cm^{-1}. Thus, the redshift in the 114.9 cm^{-1} peak is assigned to the occupancy of Bi atoms (208.9 g mol^{-1}) on Te sites (127.6 g mol^{-1}). This investigation is consistent with the XPS results of all samples (**Figure 5.3**).

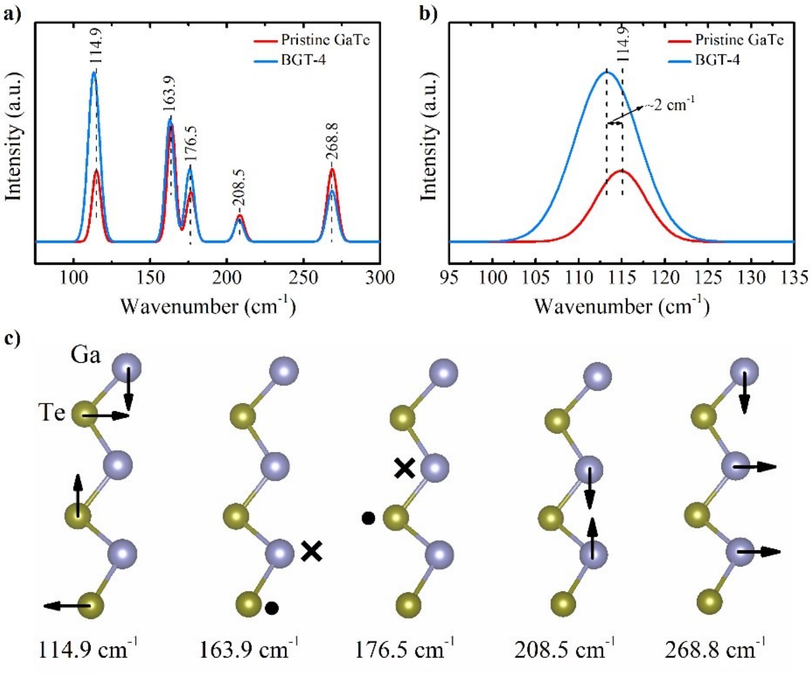

Figure 5.2: (a) Room-temperature Raman spectra for the pristine GaTe and BGT-4 samples. (b) Enlarged view of 114.9 cm^{-1} Raman peak. (c) Illustration of active modes in the monoclinic GaTe. The dark yellow and violet spheres represents the Te and Ga atoms, respectively.

The binding energies for all XPS spectra was calibrated with the C 1s peak at 284.8 eV as a reference. As shown in **Figure 5.3a**, the wide-scan spectra shows Ga 3d, Te 3d$_{5/2}$, and Te 3d$_{3/2}$ core-level peaks at 19.3, 527.7, and 583.1 eV, respectively. One negligible peak at 531.0 eV associated to the O 1s state is found, implying the oxidizing nature of GaTe. The binding energy of singlet Ga 3d peak lies between +1 and +3 oxidation states, indicating the divalent Ga cations in GaTe. No clear evidence for other oxidation states of Ga is observed. In addition, Te 3d$_{3/2}$

and Te $3d_{5/2}$ peaks are attributed to -2 oxidation states. Only one small Te^{4+} peak at 576.0 eV is indicative of TeO_2 phase existing at the surface of GaTe[80].

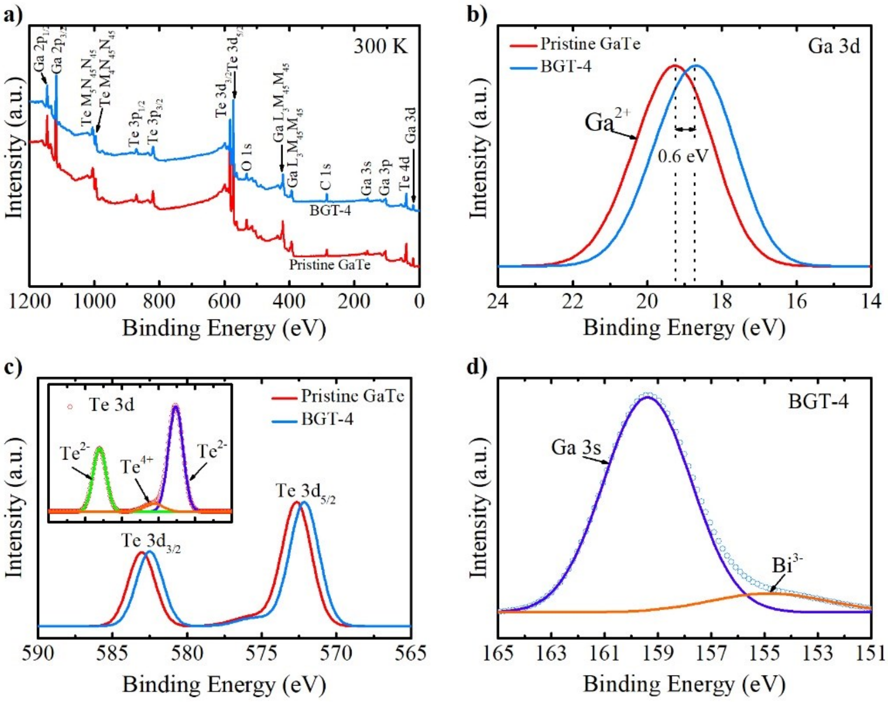

Figure 5.3: (a) Wide-scan XPS spectra of the pristine GaTe and BGT-4 samples. Narrow-scan XPS spectra for (b) Ga 3d, (c) Te 3d, and (d) Ga 3s core-level peaks. Inset shows the Gaussian fitting for the Te 3d peaks of the pristine GaTe.

As shown in **Figure 5.3b** and **Figure 5.3c**, the binding energies of Ga 3d, Te $3d_{3/2}$, and Te $3d_{5/2}$ peaks in the BGT-4 sample were downshifted by ~0.6 eV, reflecting a shift towards the valence band of Fermi level [81]. This suggest an p-type conduction in GaTe as introducing Bi atoms. Unfortunately, it is unable to point out a clear peak related to binding energy of Bi because of low doping level. However, by fitting the Ga 3s peak (**Figure 5.3d**), we found an overlapping of Ga 3s peak with a broad peak at 154.4 eV, which is lower than the binding energy of Bi metal for $4f_{7/2}$ core-level (~157.0 eV). Thus, we adopt the -3 valence for Bi atoms as occupying Te^{2-} ions, creating free holes and increasing carrier concentration.

5.2.4. Optical Band Gap

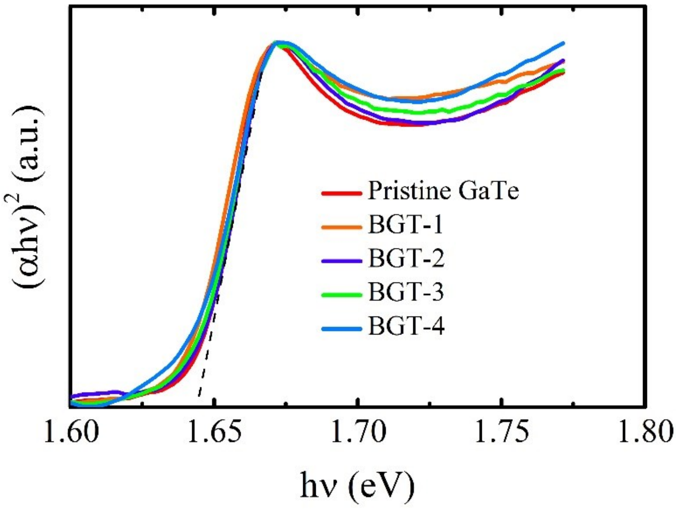

Figure 5.4: Tauc's plots from the room-temperature optical absorption spectra for all samples.

The UV-vis spectra of both samples were taken at room temperature to estimate the effect of Bi doping on the bandgap (E_g). Using the Tauc's relation, the E_g is determined from the linear extrapolation of the $(\alpha h\nu)^2$ versus $h\nu$ plots (also called Tauc's plots), as shown in **Figure 4**. Clearly, all samples have the same optical bandgap value of around 1.64 eV, demonstrating that Bi doping has no influence on the energy gap of GaTe.

5.2.5. Electrical Transport Properties

In Bi-doped GaTe samples, the increase in carrier concentration and mobility resulted in a significant improvement in electrical conductivity. The electrical conductivity rises up to 45 times, from 0.04 S cm^{-1} for pristine GaTe to 1.78 S cm^{-1} for the BGT-4 sample, as illustrated in **Figure 5.5a**. Furthermore, all samples exhibit a similar temperature variation trend, where σ increases in the temperature range of 300 - 500 K, followed by progressive decrease in the temperature range of 500 - 700 K. Typically, for the BGT-4 sample, the σ is 1.78 S cm^{-1} at 300 K, reaching a peak value of 3.62 S cm^{-1} at 500 K, then decreases to 2.13 S cm^{-1} at 700 K.

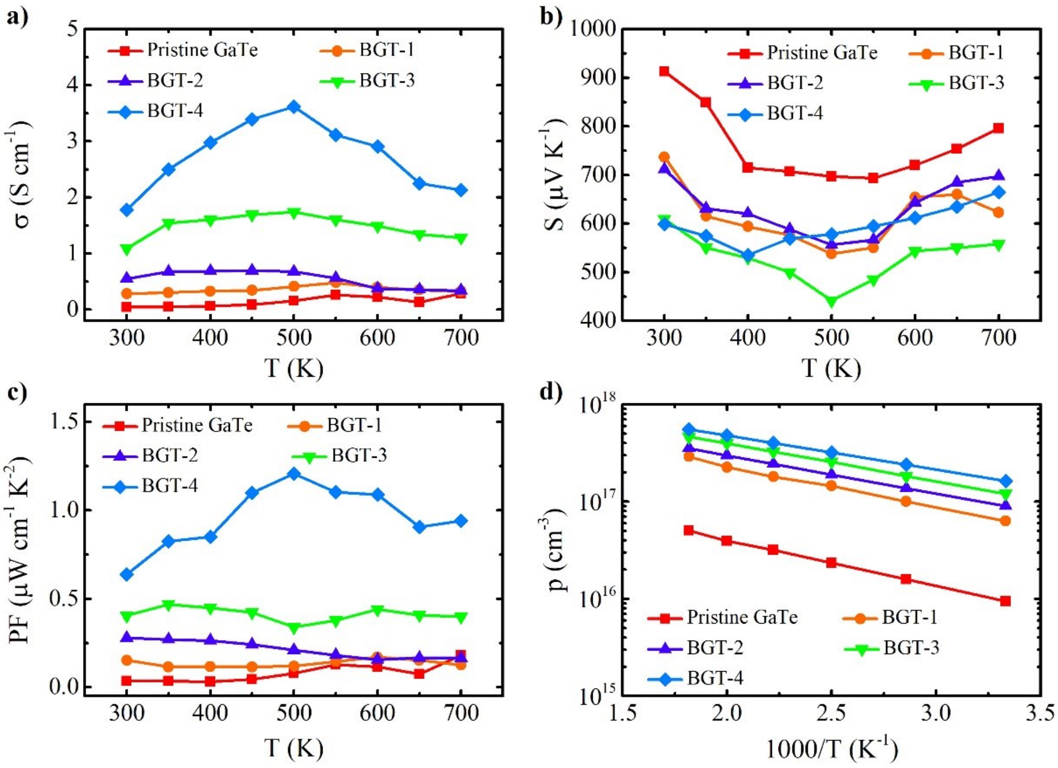

Figure 5.5: Temperature dependence (a) electrical conductivity, (b) Seebeck coefficient, and (c) thermoelectric power factor of pristine and Bi-doped GaTe samples. (d) Plots of the logarithmic scale carrier concentration versus inverse temperature for all samples.

The temperature dependency of the Seebeck coefficient S for all samples along the in-plane (ab plane) direction is shown in **Figure 5.5b**. S values are positive over the entire temperature spectrum, reflecting the dominant nature of hole carriers. This is consistent with the Hall effect measurements on the pristine and Bi-doped GaTe sample, as mentioned above. At 300 K, the pristine GaTe possesses a high Seebeck coefficient of 913 μV K^{-1}, which is comparable to the previous study of Pal *et al.*[67]. All samples show a downward trend of S with rising temperature from 300 to 500 K, then tend to increase again at higher temperatures, which is compatible with the temperature dependence of electrical conductivity. The S obviously decreases as the Bi content increases due to the rise in carrier concentration. However, the S of the Bi-doped GaTe samples remains impressively high levels even though Bi doping increases the electrical conductivity by

~45 times.

Figure 5.5c plots the dependence of the thermoelectric power factor (PF) as a function of temperature. Owing to the improved σ and the maintained large S, an enhancement in PF was achieved by the Bi doping approach. A maximum PF of ~1.21 μW cm^{-1} K^{-2} was obtained in the BGT-4 sample at 500 K, which is ~16 times higher than that of pristine GaTe.

The temperature dependence of carrier concentration was conducted in the temperature range 300 - 550 K to gain further insights into the electrical and thermal transport properties (**Figure 5.5d**). Evidently, the carrier concentration exponentially rises with increasing temperature, for example, increasing from 1.63×10^{17} cm^{-3} at 300 K to 5.49×10^{17} cm^{-3} at 550 K for the BGT-4 sample. The activation energy was calculated from the slopes of the curves using the Arrhenius equation[82]. The values of E_a are 82, 74, 68, 66, and 60 meV obtained for all samples with room temperature carrier concentrations of 0.94×10^{16}, 6.30×10^{16}, 9.00×10^{16}, 1.20×10^{17}, and 1.63×10^{17} cm^{-3}, respectively.

At the same time, all samples demonstrate a decreasing trend in carrier mobility with rising temperature, following the equation $\mu \propto T^{-1.5}$ (**Appendix A.5**), indicating the dominant acoustic-phonon scattering in the whole temperature range. Electrical conductivity and the Seebeck coefficient, in general, are highly dependent on carrier concentration and mobility, as expressed by $\sigma = ep\mu$ and $S \propto m^*/p^{2/3}$ with $\mu = e\tau/m^*$, where e is the electron charge, τ is the average scattering time, and m^* is the effective mass. Even though carrier concentration gradually increases above 500 K, carrier mobility decreases more dramatically with temperature due to improved carrier-phonon scattering. Simultaneously, the reduction in carrier mobility causes a significant temperature differential across the sample to be maintained, resulting in an increasing Seebeck coefficient.

5.2.6. Thermal Transport Properties

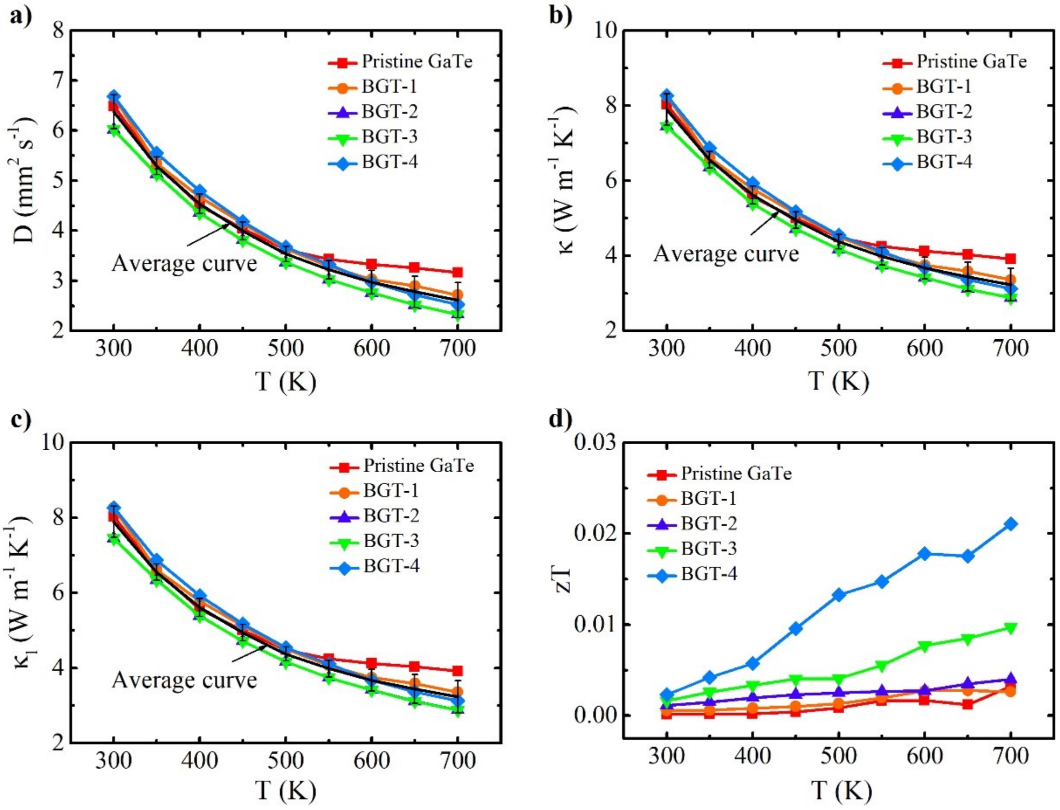

Figure 5.6: Temperature dependence of (a) thermal diffusivity, (b) total thermal conductivity, (c) lattice thermal conductivity, and (d) thermoelectric figure of merit zT for all samples.

The temperature dependence of thermal diffusivity (D) is plotted in **Figure 5.6a** for all samples. It is obvious that the D decreases monotonically over the examined temperature range of 300 - 700 K. The increased phonon scattering caused by thermal lattice vibration can explain the decrease in D with increasing temperature. Apparently, mass density ρ and specific heat capacity C_p are almost independent on the Bi doping concentration because of the low doping level. Room temperature mass density ρ and specific heat capacity C_p for all samples are evaluated to be ~5.38 ± 0.01 g cm^{-3} and ~0.23 ± 0.01 J g^{-1} K^{-1}, respectively, which are in good agreement with the previous report[83]. In this section, we will use these values to evaluate the thermal conductivity of all samples over the entire temperature range.

Figure 5.6b shows the total thermal conductivity of all samples as a function of temperature. The value for pristine GaTe (8.0 W m^{-1} K^{-1} at 300 K) is smaller than Spitzer's (8.8 W m^{-1} K^{-1}) and Milne's values (10.1 W m^{-1} K^{-1})[84,85]. Obviously, the thermal conductivity (κ) decreases with increasing temperature obeying the following law of T^{-1}, indicating that phonon-phonon scattering is dominant at high temperatures. Notably, because of the low doping concentration, Bi doping less affects the thermal conductivity of all samples. The average value for all samples is estimated to be 3.2 ± 0.4 W m^{-1} K^{-1} at 700 K. This indicates an uncertainty of $\pm 12.5\%$ for our thermal conductivity measurements. Generally, total thermal conductivity is typically defined as the sum of lattice thermal conductivity (κ_l) and electronic thermal conductivity (κ_e), i.e., $\kappa = \kappa_l + \kappa_e$. The κ_e can be determined using Wiedemann-Franz law, $\kappa_e = L\sigma T$, where L is the Lorentz number. Based on the single parabolic band model assumption, the Lorentz number is evaluated using the equation $L[10^{-8}\, V^2\, K^{-2}] = 1.5 + \exp\{-|S|/116\}$, where S is the measured Seebeck coefficient. As shown in **Appendix A.6**, the Lorentz number varies in the range of 1.50 - 1.52 $\pm$ 10^{-8} V^2 K^{-2}. Furthermore, for all samples, the electronic thermal conductivity e shows the same temperature dependence as the electrical conductivity.

As seen in **Figure 5.6c**, the lattice thermal conductivity value is very close to the total thermal conductivity because of the negligible contribution (<0.1%) of the electronic thermal conductivity. This confirms dominant role of phonons in thermal transport properties. Similarly, there is no considerable difference in lattice thermal conductivity when Te sites are replaced by Bi atoms across the entire temperature range.

The temperature tendency of the zT value of pristine and Bi-doped GaTe crystals is shown in **Figure 5.6d**. An improvement in the thermoelectric figure of merit zT is attained through an increase in electrical conductivity via Bi doping. At 700 K, the BGT-4 sample achieves a maximum zT value of up to 0.02. To the best our knowledge, this is the first experimental work to investigate the doping effects on the structural and thermoelectric properties of GaTe single crystals. Although the thermoelectric performance of Bi-doped GaTe crystals is still too low for a practical application, our findings show that Bi doping can be used to manipulate the electrical and thermal transport properties of GaTe.

5.3. Conclusion

In conclusion, using the temperature gradient method, we were able to effectively synthesize pristine and Bi-doped GaTe single crystals. The effects of Bi doping on the structural and thermoelectric properties of GaTe were studied thoroughly. Bi ions were added into the GaTe lattice, replacing the tellurium sites, and adding acceptor levels, resulting in hole carriers. The hole concentration of GaTe was increased up to 1.63×10^{17} cm^{-3} at room temperature as the Bi doping material increased, resulting in an increase in electrical conductivity. Furthermore, the crystallinity enhancement effect greatly increased carrier mobility. As a result, the BGT-4 sample obtained a maximal zT of 0.02 at 700 K, which is significantly higher than that of pristine GaTe crystals. Our findings suggested that Bi doping could be used to regulate the carrier concentration and thus increase the thermoelectric properties of GaTe. However, the solubility limit of Bi in the GaTe lattice limited the thermoelectric efficiency of Bi-doped GaTe single crystals due to the comparatively large atomic radius difference. Thus, research into other efficient dopants or dual doping should be paid to achieve high thermoelectric efficiency for GaTe systems.

Chapter 6. Summary and Outlook for GaTe-based Thermoelectric Materials

6.1. Summary

In this thesis, high-quality large-size pristine and Bi-doped GaTe single crystals were successfully synthesized for investigating the structural thermal stability and thermoelectric properties.

Particularly, we utilized a simple and effective growth method based on the "growth-from-the-melt" technique, called temperature gradient technique, for single-crystalline synthesis. To investigate the intrinsic properties, we firstly optimized the growth conditions aiming to obtain layered GaTe single crystals with high crystallinity.

Secondly, we tried to explore the structural properties and morphology of resulting crystals using XRD and SEM equipped with EDS techniques. The structural thermal stability of GaTe material was synergistically investigated through TGA and DSC analysis in various atmospheres, N_2 and Ar gases. Our findings show that GaTe is thermally stable up to 935 K in the N_2 atmosphere instead of 700 K in Ar due to the protective role of N_2 molecules on GaTe surface at high temperatures. The physical adsorption of N_2 gas is originated from the Coulomb interactions between quadrupole moments of N_2 molecules and lone-pair electrons of Te^{2-} ions in GaTe material (also known as Lewis base structure). The impact of thermal treatment on structural properties, specifically crystallinity, was systematically investigated using PL and Raman spectroscopy as a function of annealing temperature. Particularly, we found that 673 K is the optimized annealing temperature for enhancing structural thermal stability.

The third achievement is to enhance the thermoelectric properties of GaTe-based material via Bi doping. In detail, by occupying the Te^{2-} sites, Bi acceptors generate free holes, increasing the carrier concentration from 9.43×10^{15} cm^{-3} for the pristine GaTe to 1.63×10^{17} cm^{-3} for the BGT-4 sample. Moreover, the carrier mobility was increased up to 68.25 cm^2 V^{-1} s^{-1} owing to the crystallinity improvement induced by the native defect elimination role of Bi fluxes. Thus, an improvement in thermoelectric power factor, as well as zT, was achieved. In addition, the underlying mechanism of Bi doping also was systematically clarified.

6.2. Outlook on Future Research

There remain several unsolved problems associated with GaTe based thermoelectric materials.

Optimizing the carrier concentration: Even though the hole concentration of GaTe-based materials was significantly increased by ~20 times compared to the pristine sample, these values are still far from the optimal carrier concentration of 10^{19} – 10^{21} cm^{-3} for high thermoelectric efficiency. This can be explained by the low solubility limit of Bi atoms in GaTe lattice crystal due to the large atomic radius difference between doping and host atoms. Thus, a comprehensive investigation of appropriate dopants should be for further studies.

Reducing the thermal conductivity: The previous studies demonstrate that most high thermoelectric materials possess an ultralow thermal conductivity, *e.g.*, 0.4 and 0.3 W m^{-1} K^{-1} for SnSe and Cu_2Se, respectively. In this thesis, the average value of thermal conductivity for GaTe-based material is approximately 3.2 ± 0.4 W m-1 K-1 at 700 K. Thus, it demands attempts to suppress the thermal conductivity of GaTe by enhanced phonon scattering through nanostructure engineering. ***Developing two-dimensional (2D) GaTe thin films for flexible thermoelectric devices:*** According to recent theoretical papers, reducing GaTe's thickness to monolayer level would greatly improve the material's electrical conductivity. Although there is a severe lack of literature on 2D GaTe thin films. In addition, in recent years, there has been a significant increase in the market for lightweight, environmentally friendly, and flexible devices that can produce electricity from body heat. Hence, the synthesis and thermoelectric properties of GaTe monolayers should be considered.

List of Abbreviations

2D	Two Dimensional
DSC	Differential Scanning Calorimetry
EDS	Dispersive Energy Spectroscopy
FE-SEM	Field Emission Scanning Electron Microscopy
LFA	Laser Flash Analysis
PF	Power Factor
PL	Photoluminescence
TE	Thermoelectric
TECs	Thermoelectric Coolers
TEGs	Thermoelectric Generators
TGA	Thermogravimetry Analysis
UV-vis	Ultraviolet-visible
vdP	van der Pauw
vdW	van der Waals
XPS	X-ray Photoelectron Spectroscopy
XRD	X-ray Diffraction

A. Appendix

A.1. Derivative Weight Thermometric (DTG)

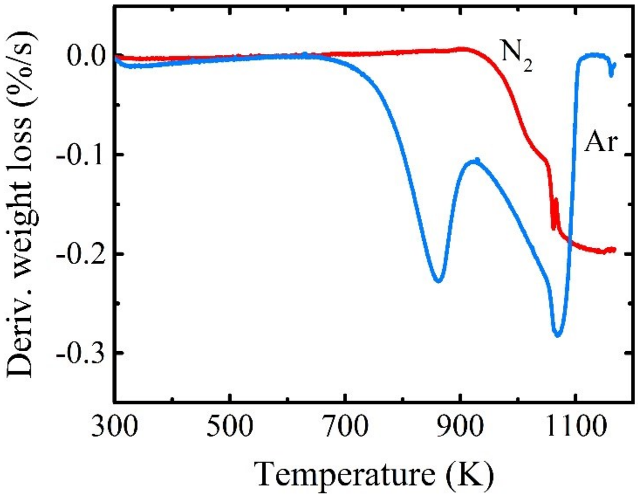

A.2. Plot of Hall Coefficient versus Magnetic Field

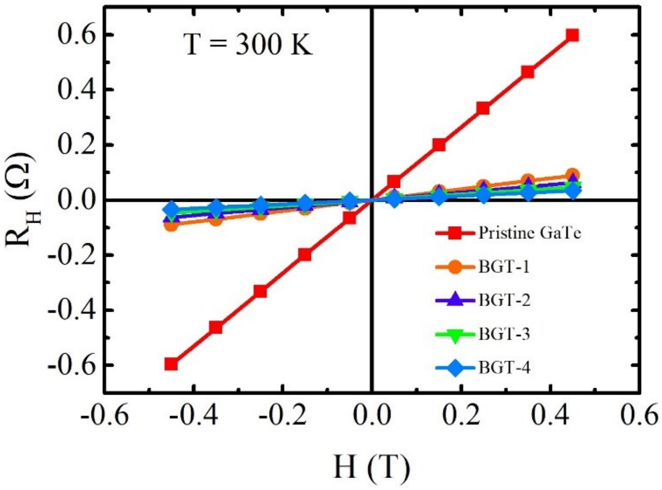

A.3. Dependence of Carrier Concentration on Sample Length

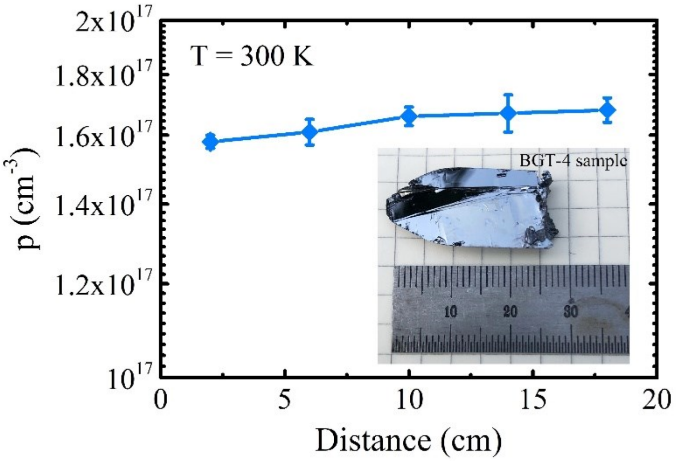

A.4. PL Intensity as a Function of Doping Carrier Concentration

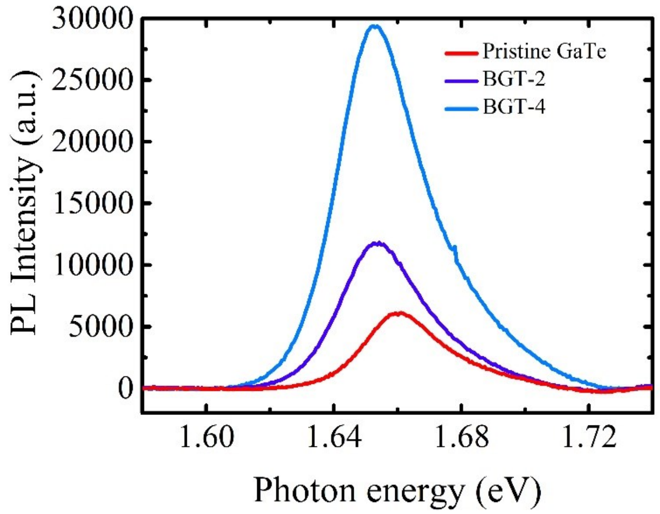

A.5. Temperature Dependence of Carrier Mobility

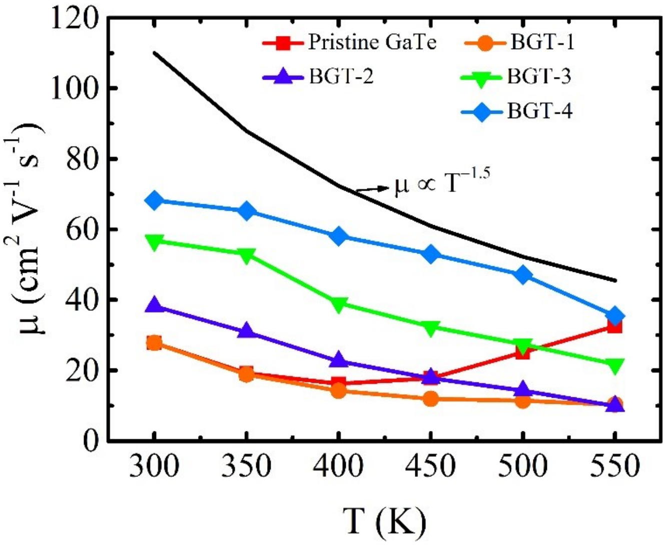

A.6. Temperature Dependence of Lorentz Number and Electronic Thermal Conductivity

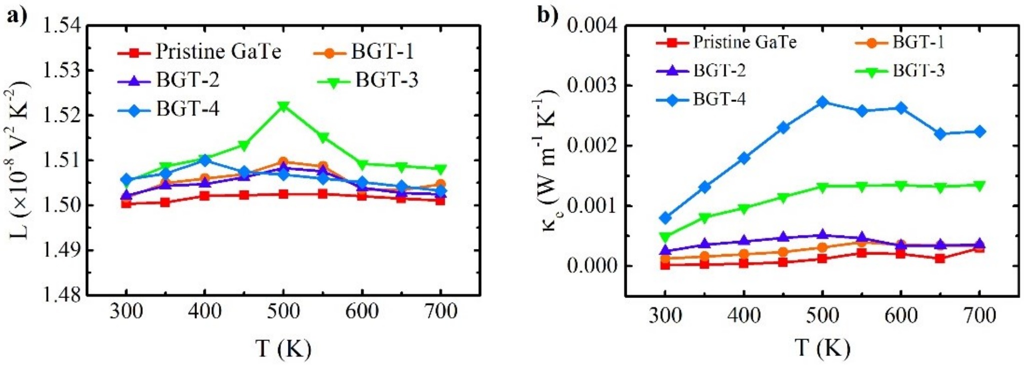

References

[1] X. Zhang and L.-D. Zhao, J. Materiomics **1**, 92 (2015).

[2] J.J. Gutiérrez Moreno, J. Cao, M. Fronzi, and M.H.N. Assadi, Mater. Renew. Sustain. Energy. **9**, 16 (2020).

[3] P. Ying, R. He, J. Mao, Q. Zhang, H. Reith, J. Sui, Z. Ren, K. Nielsch, and G. Schierning, Nat. Commun. **12**, 1121 (2021).

[4] W. Liu, Q. Jie, H.S. Kim, and Z. Ren, Acta Mater. **87**, 357 (2015).

[5] R. He, G. Schierning, and K. Nielsch, Adv. Mater. Technol. **3**, (2018).

[6] C.-C. Wang, C.-I. Hung, and W.-H. Chen, Energy **39**, 236 (2012).

[7] N. Jaziri, A. Boughamoura, J. Müller, B. Mezghani, F. Tounsi, and M. Ismail, Energy Rep. **6**, 264 (2020).

[8] J. Yu, Q. Zhu, L. Kong, H. Wang, and H. Zhu, Energies **13**, 4691 (2020).

[9] H.S. Kim, W. Liu, G. Chen, C.W. Chu, and Z. Ren, Proc. Natl. Acad. Sci. U.S.A. **112**, 8205 (2015).

[10] G.J. Snyder and E.S. Toberer, Nat. Mater. **7**, 105 (2008).

[11] P. Pichanusakorn and P. Bandaru, Mater. Sci. Eng. R Rep. **67**, 19 (2010).

[12] A. Zunger, Appl. Phys. Lett. **83**, 57 (2003).

[13] Y. Yan, S.B. Zhang, and S.T. Pantelides, Phys. Rev. Lett. **86**, 5723 (2001).

[14] M.W. Oh, J.H. Son, B.S. Kim, S.D. Park, B.K. Min, and H.W. Lee, J. Appl. Phys. **115**, 13 (2014).

[15] S.S. Li, in *Semiconductor Physical Electronics*, edited by S.S. Li (Springer New York, New York, NY, 2006), pp. 211–245.

[16] Y.L. Pei, H. Wu, D. Wu, F. Zheng, and J. He, J. Am. Chem. Soc. **136**, 13902 (2014).

[17] Y. Pei, A.D. Lalonde, H. Wang, and G.J. Snyder, Energy Environ. Sci. **5**, 7963 (2012).

[18] Y. Takagiwa, Y. Pei, G. Pomrehn, and G.J. Snyder, Appl. Phys. Lett. **101**, 1 (2012).

[19] H. Wang, H. Hu, N. Man, C. Xiong, Y. Xiao, X. Tan, G. Liu, and J. Jiang, Mater. Today Phys. **16**, 100298 (2021).

[20] Y. Pei, X. Shi, A. Lalonde, H. Wang, L. Chen, and G.J. Snyder, Nature **473**, 66 (2011).

[21] H. Sitter, K. Lischka, and H. Heinrich, Phys. Rev. B **16**, 680 (1977).

[22] Y. Pei, A.D. Lalonde, N.A. Heinz, X. Shi, S. Iwanaga, H. Wang, L. Chen, and G.J. Snyder, Adv. Mater. **23**, 5674 (2011).

[23] D. Sarkar, T. Ghosh, A. Banik, S. Roychowdhury, D. Sanyal, and K. Biswas, Angew. Chem. Int. **59**, 11115 (2020).

[24] Y. Feng, J. Li, Y. Li, T. Ding, C. Zhang, L. Hu, F. Liu, W. Ao, and C. Zhang, J. Mater. Chem. A **8**, 11370 (2020).

[25] X. Sun, X. Li, J. Yang, J. Xi, R. Nelson, C. Ertural, R. Dronskowski, W. Liu, G.J. Snyder, D.J. Singh, and W. Zhang, J. Comput. Chem. **40**, 1693 (2019).

[26] K. Imasato, S.D. Kang, S. Ohno, and G.J. Snyder, Mater. Horiz. **5**, 59 (2018).

[27] J. Zhai, T. Wang, H. Wang, W. Su, X. Wang, T. Chen, and C. Wang, Chin. Phys. B **27**, 047306 (2018).

[28] L.-D. Zhao, S.-H. Lo, Y. Zhang, H. Sun, G. Tan, C. Uher, C. Wolverton, V.P. Dravid, and M.G. Kanatzidis, Nature **508**, 373 (2014).

[29] Y.-L. Pei, J. He, J.-F. Li, F. Li, Q. Liu, W. Pan, C. Barreteau, D. Berardan, N. Dragoe, and L.-D. Zhao, NPG Asia Mater. **5**, e47 (2013).

[30] X. Li, P.-F. Liu, E. Zhao, Z. Zhang, T. Guidi, M.D. Le, M. Avdeev, K. Ikeda, T. Otomo, M. Kofu, K. Nakajima, J. Chen, L. He, Y. Ren, X.-L. Wang, B.-T. Wang, Z. Ren, H. Zhao, and F. Wang, Nat. Commun. **11**, 942 (2020).

[31] J.-Y. Tak, W.H. Nam, C. Lee, S. Kim, Y.S. Lim, K. Ko, S. Lee, W.-S. Seo, H.K. Cho, J.-H. Shim, and C.-H. Park, Chem. Mater. **30**, 3276 (2018).

[32] X. Shi, L. Chen, and C. Uher, Int. Mater. Rev. **61**, 379 (2016).

[33] M. Samanta, T. Ghosh, S. Chandra, and K. Biswas, J. Mater. Chem. A **8**, 12226 (2020).

[34] M. Sajjad, Q. Mahmood, N. Singh, and J. Andreas Larsson, ACS Appl. Energy Mater. **3**, 11293 (2020).

[35] V.P. Gupta and V.K. Srivastava, J. Phys. Chem. Solids **42**, 1071 (1981).

[36] H. Shangguan, L. Han, T.A.O. Zhang, R. Quhe, Q. Wang, S. Li, and P. Lu, J. Electron. Mater. **48**, 5988 (2019).

[37] K.C. Mandal, S. Das, R. Krishna, P.G. Muzykov, S. Ma, and F. Zhao, Mater. Res. Soc. Symp. Proc. Vol. **1268**, 2 (2010).

[38] K. Lee, S. Kamali, T. Ericsson, M. Bellard, and K. Kovnir, Chem. Mater. **28**, 2776 (2016).

[39] N.N. Kolesnikov, E.B. Borisenko, D.N. Borisenko, and A. V. Timonina, J. Cryst. Growth **365**, 59 (2013).

[40] S. Huang, Y. Tatsumi, X. Ling, H. Guo, Z. Wang, G. Watson, A.A. Puretzky, D.B. Geohegan, J. Kong, J. Li, T. Yang, R. Saito, and M.S. Dresselhaus, ACS Nano **10**, 8964 (2016).

[41] T. Wang, Q. Zhao, Y. Miao, F. Ma, Y. Xie, and W. Jie, Crystals **8**, (2018).

[42] V.N. Brudnyi, S.Y. Sarkisov, and A. V Kosobutsky, Semicond. Sci. Technol. **30**, 115019 (2015).

[43] D. Feng, Z.-H. Ge, D. Wu, Y.-X. Chen, T. Wu, J. Li, and J. He, Phys. Chem. Chem. Phys. **18**, 31821 (2016).

[44] X. Wang, J. Xu, G.-Q. Liu, X. Tan, D. Li, H. Shao, T. Tan, and J. Jiang, NPG Asia Mater. **9**, e426 (2017).

[45] D. Liu, X. Li, P.M. de C. Borlido, S. Botti, R. Schmechel, and M. Rettenmayr, Sci. Rep. **7**, 43611 (2017).

[46] R.L. González-Romero, A. Antonelli, A.S. Chaves, and J.J. Meléndez, Phys. Chem. Chem.

Phys. **20**, 1809 (2018).

[47] K. Mori, H. Usui, H. Sakakibara, and K. Kuroki, AIP Adv. **2**, 42108 (2012).

[48] E.B. Isaacs and C. Wolverton, Phys. Rev. Mater. **3**, 15403 (2019).

[49] B.P. Bahuguna, L.K. Saini, R.O. Sharma, and B. Tiwari, Phys.Chem.Chem.Phys. **20**, 28575 (2018).

[50] M.-S. Li, K.-X. Chen, D.-C. Mo, and S.-S. Lyu, Phys.Chem.Chem.Phys. **21**, 24695 (2019).

[51] H. Efeo lu, T. Karacali, B. Abay, and Y.K. Yo urtçu, Semicond. Sci. Technol. **19**, 523 (2004).

[52] S. Shigetomi, T. Ikari, and H. Nakashima, Jpn. J. Appl. Phys. **37**, 3282 (1998).

[53] S. Pal and D. Bose, Solid State Commun. **97**, 725 (1996).

[54] K.C. Mandal, R.M. Krishna, T.C. Hayes, P.G. Muzykov, S. Das, T.S. Sudarshan, and S. Ma, IEEE Trans. Nucl. Sci. **58**, 1981 (2011).

[55] Y. Ren, Q. Jiang, J. Yang, Y. Luo, D. Zhang, Y. Cheng, and Z. Zhou, J. Materiomics **2**, 172 (2016).

[56] H. Kim, K.H. Lee, J. Yoo, J. Youn, J.W. Roh, S. Kim, and S.W. Kim, Materials **10**, (2017).

[57] F. Liu, M. Wang, Y. Chen, and J. Gao, J. Solid State Chem. **276**, 100 (2019).

[58] H.Y. Nan, Z.H. Ni, J. Wang, Z. Zafar, Z.X. Shi, and Y.Y. Wang, J. Raman Spectrosc. **44**, 1018 (2013).

[59] X.-S. Liang, J.-H. Ouyang, and Z.-G. Liu, J. Therm. Anal. Calorim. **111**, 371 (2013).

[60] C. Barreteau, D. Berardan, and N. Dragoe, J. Solid State Chem. **222**, 53 (2015).

[61] K. Yin, Q. Zhang, Y. Zheng, X. Su, X. Tang, and C. Uher, J. Mater. Chem. C **3**, 10381 (2015).

[62] E. Mercado, Y. Zhou, Y. Xie, Q. Zhao, H. Cai, B. Chen, W. Jie, S. Tongay, T. Wang, and M. Kuball, ACS Omega **4**, 18002−18010 (2019).

[63] M. Kotha, T. Murray, D. Tuschel, and S. Gallis, Nanomaterials **9**, 1510 (2019).

[64] J.J. Fonseca, S. Tongay, M. Topsakal, A.R. Chew, A.J. Lin, C. Ko, A. V Luce, A. Salleo, J. Wu, and O.D. Dubon, Adv. Mater. **28**, 6465 (2016).

[65] D.T.J. Hurle, in *J. Appl. Cryst.* (John Wiley & Sons Ltd, 1994), p. 55.

[66] T.H. Vu, A.T. Pham, V.Q. Nguyen, A.D. Nguyen, T.N. Nguyen Tran, M.H. Nguyen Thi, Y.S. Kim, V.T. Tran, and S. Cho, J. Solid State Chem. **296**, 121996 (2021).

[67] S. Pal and D.N. Bose, Bull. Mater. Sci. **17**, 1039 (1994).

[68] F. Liu, H. Shimotani, H. Shang, T. Kanagasekaran, V. Zolyomi, N. Drummond, V.I. Falko, and K. Tanigaki, ACS Nano **8**, 752 (2014).

[69] D.N. Bose and S. Pal, Phys. Rev. B **63**, 235321 (2001).

[70] Y. Cui, D.D. Caudel, P. Bhattacharya, A. Burger, K.C. Mandal, D. Johnstone, and S.A. Payne, J. Appl. Phys. **105**, 053709 (2009).

[71] P. Hu, J. Zhang, M. Yoon, X.F. Qiao, X. Zhang, W. Feng, P. Tan, W. Zheng, J. Liu, X.

Wang, J.C. Idrobo, D.B. Geohegan, and K. Xiao, Nano Res. **7**, 694 (2014).

[72] C. Spindler, T. Galvani, L. Wirtz, G. Rey, and S. Siebentritt, J. Appl. Phys. **126**, 175703 (2019).

[73] S.T. Wang, F. Ma, X. Ma, P. Chem, and C. Phys, Phys. Chem. Chem. Phys. **18**, 18719 (2016).

[74] A. Yamamoto, A. Syouji, T. Goto, E. Kulatov, K. Ohno, Y. Kawazoe, K. Uchida, and N. Miura, Phys. Rev. B **64**, 035210 (2001).

[75] N. Gupta and A. Khanna, J. Non-Cryst. Solids **481**, 594 (2018).

[76] C. Kranert, C. Sturm, R. Schmidt-Grund, and M. Grundmann, Sci. Rep. **6**, 35964 (2016).

[77] R.E. Honig, in *RCA Rev.* (1957), pp. 195–204.

[78] T.H. Vu, A.T. Pham, V.Q. Nguyen, J. Park, S. Park, and S. Cho, J. Solid State Chem. 122155 (2021).

[79] J. Susoma, J. Lahtinen, M. Kim, J. Riikonen, and H. Lipsanen, AIP Adv. **7**, 015014 (2017).

[80] S. Yang, H. Cai, B. Chen, C. Ko, V.O. Özçelik, D.F. Ogletree, C.E. White, Y. Shen, and S. Tongay, Nanoscale **9**, 12288 (2017).

[81] R. Zhang, D. Drysdale, V. Koutsos, and R. Cheung, Adv. Funct. Mater. **27**, 1702455 (2017).

[82] F. Jensen, Qual. Reliab. Eng. Int. **1**, 13 (1985).

[83] A. V Tyurin, K.S. Gavrichev, V.P. Zlomanov, and N.N. Smirnova, Inorg. Mater. **42**, 855 (2006).

[84] W.I. Milne, J.C. Anderson, R.L. Hargreaves, P.R. Mason, C. Paorici, N. Romeo, and L. Tarricone, J. Phys. D: Appl. Phys. **6**, 2115 (1973).

[85] D.P. Spitzer, J. Phys. Chem. Solids **31**, 19 (1970).

Curriculum Vitae

PERSONAL DETAILS

Full name: Thi Hoa Vu

Date of birth: 1992-08-20

Nationality: Vietnamese

ORCID: 0000-0001-6507-7242

Address: Department of Physics, University of Ulsan
93, Daehak-ro, Nam-gu, Ulsan, 44610, South Korea

Tel: (+82) 010-9513-2008

Email: nguyen.vu.hnue@gmail.com

PROFILE

Thi Hoa Vu has a scientific background in physics and chemistry. She has broad experience in the synthesis and characterizes the structural and thermoelectric properties of van der Waals (vdW) layered materials, such as $SnSe_2$, GaTe, $(Bi, Sb)_2(Se, Te)_3$ based systems. She has six years of experience in "growth-from-the-melt" techniques for designing and controlling the electrical and thermal transport properties of layered materials. In addition, she also has experiences on material characterization using x-ray diffraction, scanning electron microscope, x-ray photoelectron spectroscopy, photoluminescence, Raman spectroscopy, and thermogravimetry analysis.

ACADEMIC DEGREES

2015-present: Ph.D. in Department of Physics, University of Ulsan, Ulsan 44610, South Korea. Supervisor: Sunglae Cho

2010-2014: Bachelor in Faculty of Physics, Hanoi National University of Education (HNUE), Hanoi 10000, Vietnam. Supervisor: Quang Hoc Nguyen

PUBLICATIONS

1. Pham, A.-T.; **Vu, T. H**.; Cheng, C.; Trinh, T. L.; Lee, J.-E.; Ryu, H.; Hwang, C.; Mo, S.-K.; Kim, J.; Zhao, L.; Duong, A.-T.; Cho, S. High-Quality SnSe2 Single Crystals: Electronic and Thermoelectric Properties. *ACS Appl. Energy Mater.* **2020**, *3* (11), 10787–10792.
2. **Vu, T. H.**; Pham, A. T.; Nguyen, V. Q.; Nguyen, A. D.; Nguyen Tran, T. N.; Nguyen Thi, M. H.; Kim, Y. S.; Tran, V. T.; Cho, S. Growth and Thermal Stability Studies of Layered GaTe Single Crystals in Inert Atmospheres. *J. Solid State Chem.* **2021**, *296*, 121996.
3. Pham, A.-T.; **Vu, T. H**.; Nguyen, Q. V; Vu, M. T.; Park, J. H.; Park, S.-D.; Cho, S. Br-Doped n-Type SnSe2: Single-Crystal Growth and Thermoelectric Properties. *ACS Appl. Energy Mater.* **2021**, *4* (3), 2908–2913.
4. **Vu, T. H.**; Pham, A. T.; Nguyen, V. Q.; Park, J.; Park, S.; Cho, S. Bi-Doped GaTe Single Crystals: Growth and Thermoelectric Properties. *J. Solid State Chem.* **2021**, 122155.

REFERENCES

1. **Prof. Sunglae Cho,** Department of Physics and Energy Harvest-Storage Research Center, University of Ulsan, Ulsan 44610, South Korea.
   Email: slcho@ulsan.ac.kr
   Tel: (+82) 052-259-2322
2. **Dr. Van Quang Nguyen,** Department of Physics and Energy Harvest-Storage Research Center, University of Ulsan, Ulsan 44610, South Korea.
   Email: quang3012@ulsan.ac.kr
   Tel: (+82) 010-9723-1210
3. **Prof. Quang Hoc Nguyen,** Faculty of Physics, Hanoi University of Education, 136 Xuan Thuy, Cau Giay, Hanoi 10000, Vietnam.
   Email: hocnq@hnue.edu.vn
   Tel: (+84) 043-837-0428